DESIGN, IMPLEMENTATION AND CONSTRUCTION OF AN EIGHT CHANNEL RF TEM ARRAY AND ITS USE IN MR-EPT

A THESIS SUBMITTED TO

THE GRADUATE SCHOOL OF ENGINEERING AND SCIENCE

OF BILKENT UNIVERSITY

IN PARTIAL FULFILLMENT OF THE REQUIREMENTS FOR

THE DEGREE OF

MASTER OF SCIENCE

IN

ELECTRICAL AND ELECTRONICS ENGINEERING

By

Gökhan Arıtürk

July 2018

Design, Implementation and Construction of an Eight Channel RF TEM Array and Its Use in MR-EPT
By Gökhan Arıtürk
July 2018

We certify that we have read this thesis and that in our opinion it is fully adequate, in scope and in quality, as a thesis for the degree of Master of Science.

Yusuf Ziya Ider(Advisor)

Ergin Atalar

Birsen Saka Tanatar

Approved for the Graduate School of Engineering and Science:

Ezhan Karaşan
Director of the Graduate School

ABSTRACT

DESIGN, IMPLEMENTATION AND CONSTRUCTION OF AN EIGHT CHANNEL RF TEM ARRAY AND ITS USE IN MR-EPT

Gökhan Arıtürk
M.S. in Electrical and Electronics Engineering
Advisor: Yusuf Ziya Ider
July 2018

Magnetic Resonance – Electrical Properties Tomography, aiming at reconstructing the electrical properties (EPs) at radio frequencies, has a continuously increasing importance in terms of identifying the cancerous tissues and distinguishing between ischemic and hemorrhagic stroke. The presently prominent MR-EPT method "Convection–Reaction Equation Based MR-EPT" is still not clinically used due to the presence of image artifacts. In this regard, the objective of this thesis is to eliminate the low convective field (LCF) artifact, which refers to abrupt and point-wise image perturbations on the conductivity and permittivity reconstructions of cr-MREPT method. Since the proposed methods involve the use of parallel RF transmission, a multichannel transceiver array is designed by carefully scrutinizing the original TEM resonator, proposed by J.Thomas Vaughan in 1994. Finite Element Method (FEM) based simulations of that structure, which includes the use of coaxial line elements (transmission lines), are done in Comsol Multiphysics. For better practical feasibility, a microstrip transmission line based eight–channel TEM array was designed, simulated and constructed. Each of the eight ports of this array is matched to 50 Ω with reflection coefficients as low as -40 dB at 123.2 MHz. Worst decoupling between the ports is measured as -14 dB. With the use of quadrature excitation, clear MRI images of experimental phantoms and highly homogeneous B_1^+ maps are obtained. Using simulations, a method to eliminate the LCF artifact from the EP reconstructions is proposed. This method involves the use of the TEM array in two different excitation configurations. In the first excitation, the conventional quadrature drive is used. The second excitation, on the other hand, uses magnitude and phase optimized RF sinusoids to produce a proper transmit field (B_1^+) within the object. This intentionally adjusted (B_1^+) field, which comprises high field and low field regions with a transition in the middle, shifts the LCF

artifact towards a non-central location. Finally, data from both drive experiments are simultaneously used to reconstruct EP's. It has been further shown that the method can be applied to different patients without requiring patient-specific B_1^+ optimizations. Experimentally implementing the proposed method, another novel algorithm to extract the phase of the transmit field ($\phi_{B_1^+}$) in a non-quadrature excitation is proposed. In this algorithm, the receive phases of individual channels, being common for quadrature and non-quadrature experiments are found from an additional quadrature drive experiment with the use of transceive phase assumption. Then, the transmit phase of non-quadrature drive is extracted by subtracting the receive phases from the transceive phase distributions. Strong consensus between the simulated and experimentally estimated transmit phases is observed. In conclusion, the conductivity reconstructions of an experimental phantom, with the use of the developed methods, is provided. It has been shown that the LCF artifact is alleviated and better experimental setups are required to fully eliminate it.

Keywords: RF Coil, RF Transceiver Array, TEM Coil, MR-EPT, B_1 Shimming.

ÖZET

SEKİZ KANALLI RF TEM SARIM DİZAYNI, ÜRETİMİ VE MREÖT ÇALIŞMALARINDA KULLANIMI

Gökhan Arıtürk
Elektrik Elektronik Mühendisliği, Yüksek Lisans
Tez Danışmanı: Yusuf Ziya Ider
Temmuz 2018

Günümüzde hızla yaygınlaşmakta olan "Manyetik Rezonans Elektriksel Özellik Tomografisi" adlı çalışmalar; dokuların yüksek frekanslardaki elektriksel özelliklerini görüntüleyerek kanserli bölgelerin teşhisinde ve ayrıca, iskemik ve hemorojik inme arasında ayrım yapılmasında önemli rol almaktadır. Bu konudaki en önemli çalışmalardan olan cr-MREPT, ortaya çıkan görüntü artefaktları sebebiyle klinik çalışmalarda kullanılamamaktadır. Bu bağlamda hazırlanan tez, "Düşük Konvektif Bölge (DKB) Artefaktı" denilen ve elektriksel iletkenlik görüntülerinde ani ve yersiz sıçramalara sebep olan görüntü artefaktının düzeltilmesini amaçlamaktadır. Paralel RF gönderiminin kullanılması sebebiyle kullanılacak olan çok kanallı bir TEM sarımın tasarımı; 1994 yılında J. Thomas Vaughan tarafından dizayn edilen orjinal sarımın derinlemesine incelenmesiyle başlatılmaktadır. Koaksiyel elemanların kullanıldığı bu karmaşık yapı, sonlu elemanlar ağı (FEM) metodu kullanılarak Comsol Multiphysics ortamında simüle edilmiştir. Daha kolay uygulanabilir olduğu için, microstrip eleman bazlı bir TEM sarımı tasarlanıp üretilmiştir. Bu sarımın portları 50 Ω 'luk bir empedansa eşlendikten sonra elde edilen yansıma katsayıları 123.2 MHz'de -40dB dolaylarında olmakla birlikte en kötü izolasyon, -14 dB olarak ölçülmüştür. Üretilen bu sarım quadrature olarak sürüldüğünde, az gürültülü MRI görüntüleri ve oldukça homojen B_1 haritaları elde edilmiştir. Bunun ardından, DKB artefaktını ortadan kaldırabilmek için simülasyon temelli özgün bir yöntem ortaya atılmıştır.Bu yöntem, tasarlanan TEM sarımını iki farklı sürme durumunda kullanmayı içermektedir. İlk sürme durumu, MRI sistemlerinde standart olarak kullanılan "quadrature" adlı sürme konfigürasyonudur. İkinci sürme durumunda ise portlardan uygulanan RF sinyallerin genlik ve fazları; sarımın içerisinde istenilen manyetik alanı üretebilecek şekilde tasarlanmıştır. İkinci sürmede kullanılan bu manyetik alan, DKB artefaktını merkezden uzaklaştıracak şekilde

kaydırmaktadır. Sonuçta ise, her iki sürme durumundan elde edilen B_1^+ verileri birlikte kullanılarak cr-MREPT denklemleri çözülmüş ve artefakttan arındırılmış temiz bir iletkenlik görüntüsüne ulaşılmıştır. Buna ek olarak, RF sarımlarda gönderme fazını bulabilmek için özgün bir metot daha önerilmiş olup, önerilen bu metotla MRI deneylerinden iletkenlik görüntüleri elde edilmiştir. Buna ek olarak, elde edilen yöntemi kullanabilmek için her hastaya özel B_1 optimizasyonuna ihtiyaç duyulmamaktadır. Bu yöntemi deneylerde kullanabilmek için ise gönderme fazını (B_1^+); non-quadrature sürme durumlarında bulabilmek için ayrı bir metot sunulmuştur. Bu metotta, her kanal için her sürme durumunda aynı olan alma fazları, ek bir quadrature sürme deneyi ve TPA varsayımı kullanılarak bulunmaktadır. Bulunan bu alma fazları her bir kanala gelen toplam fazdan çıkarılarak gönderme fazına ulaşılmaktadır. Bu bağlamda, simülasyonlarda ve deneylerde bulunan gönderme fazlarının oldukça benzer çıktığı gözlemlenmektedir. Sonuç olarak ise deneysel bir fantomun; bütün bu metotlar kullanılarak iletkenlik görüntüleri alınmaktadır. Görüntülerde her ne kadar DKB artefaktı kısmen ortadan kaldırılmış olsa da daha iyi bir RF/MRI sistemi kullanılarak bu artefaktın ortadan kaldırılabileceği tartışılmaktadır.

Anahtar sözcükler: RF Sarım, RF Gönderme/Alma Sarımı, TEM Sarımı, MR-EÖT, B_1 Ayarlama .

Acknowledgement

Considering my research experience, my studies and the previous three years, I would like to express my sincere appreciation and gratitude to my graduate supervisor Prof. Yusuf Ziya Ider. Aside from his guidance and caring attitude towards our group, he instilled numerous essential life attitudes to us, which I believe, cannot be acquired from any other occupation. I would like to emphasize the role of his complete honesty and his extreme perseverance for success, in the context of teaching me the act of striving for victory, even in the worst scenerio.

I need to thank to Prof. Ergin Atalar and Prof. Birsen Saka for accepting to be my judges in my thesis defence.

I would like to thank so much for Prof. Ergin Atalar and his research team, including Taner Demir, Umut Gündoğdu, Ali Reza Sadeghi Tarakmeh, Berk Silemek, Mustafa Can Delikanlı, and Volkan Açıkel for their help and guidance in the use of the MRI system located in UMRAM. I would also like to thank to Dr. Hulusi Kafaligönül and Dr. Ceyhun Bulutay for their support and guidance.

I appreciate the collaboration and help of Prof. Vakur Behçet Ertürk in the context of electromagnetic theory.

Very special thanks to the members of our team, including Yiğit Tuncel, Toygun Başaklar, Gülşah Yıldız, Çelik Boğa, Safa Özdemir, Necip Gürler and Ömer Oran for developing a spirit of teamwork in our research group.

I appreciate the lovely friendship and endless support of Erhan Erköseoğlu, Alp Emek, Özge Şener, Çağatay Gürsoy and Mert Yüksel, who thoroughly supported me during my studies. I believe that I owe a lot to them.

Finally, I wish to express my inexplicable gratitude to my parents Nazan & Orhan Arıtürk for their immaterial and tangible support. I can definitely state that not only the completion of this study, but also this entire life would have been horrendously more difficult without them.

Contents

List of Figures

List of Tables

Chapter 1

Introduction

Contemporarily, the increasing need for enhanced tissue images with the highly interdisciplinary imaging method "Magnetic Resonance Imaging" (MRI) has led many researchers from different backgrounds (i.e. physics, chemistry, engineering, medicine) to collaboratively work in order for pushing its limits. With the use of three main magnetic fields, this highly convoluted imaging method spans many different areas of electromagnetic theory and applied electromagnetics. Demonstrating the pertinence of MRI to the different areas of applied electromagnetics, therefore, our departure point would be the main magnetic fields used in MRI. They can be stated as:

- $\boldsymbol{B_0}$: The main static and spatially constant/homogeneous magnetic field, generated by a high power dc-current. This field is used to direct the initial magnetization vector inside the biological tissue towards the $z-direction$.
- G_x, G_y, G_z: The low frequency, high power gradient fields which are space dependent and generated by the gradient coils. The gradient fields are used for slice selection and for travelling through the k-space.
- $\boldsymbol{B_1}$: The high frequency (generally in MHz range) polarized magnetic field which is generated by the radio frequency (RF) coils. This field is used for flipping the z-directed magnetization vector towards the transverse plane

($x - y$ plane). This action can also be called as "exciting" the biological tissue to be imaged.

In the scope of this thesis, we have been extensively dealing with the generation of the high frequency field ($\boldsymbol{B_1}$) and its use for electrical property imaging. In this regard, scientific background of the two major concepts of this thesis, being the *RF Coils* and *Electrical Tissue Mapping* is given in the following introductory sections.

1.1 RF Coils Used in MRI

Just like in a commercial RF transceiver system such as radio, wi-fi or radar, RF coils and antennas are used for tranmission and signal reception in MRI applications. The "transmitter" coils are supposed to generate the $\boldsymbol{B_1}$ field that flips the z-directed magnetizations within the tissue to be imaged by transmitting an RF signal towards its interior. After transmission of the RF waveform, the *receiver* coils are designed to *collect* the induced RF currents on themselves, which is caused by the recovery (flipping back towards the z-direction) of the pre-excited spins.

The $\boldsymbol{B_1}$ field comprises a clockwise (B_1^+) and another counter-clockwise (B_1^-) circularly polarized magnetic field. These components of the high frequency magnetic field turn out to be highly important in the environment of MRI. The clockwise-polarized magnetic field (B_1^+) is defined as the *transmit field* and the complex conjugate of the counter-clockwise polarized field (B_1^{-*}) gives us the *receive field*, as previously described [2]. The definition of these circularly polarized fields, in terms of the actual magnetic field intensity are given as in the following:

$$B_1^+ = \frac{(B_x + iB_y)}{2} = \frac{\mu_0(H_x + iH_y)}{2}$$
$$B_1^- = \frac{(B_x - iB_y)^*}{2} = \frac{\mu_0(H_x - iH_y)^*}{2} \tag{1.1}$$

While the transmission and reception processes can be accomplished by a single *transceiver coil*, there are transmit only and receive only coils used in different applications.

1.1.1 RF Volume Coils

The term "volume coil" is used for the ones that transmit towards a particular volume, which is generally the interior region of the coil structure. The most ubiquitously used RF transmit volume coils are the birdcage, phased array and transverse electromagnetic (TEM) coils, which can also be used for reception. Even though these coils have the capability of RF reception, many commercial MRI systems employ the receive-only coils such as surface coils and receive-only phased arrays for enhancing the signal to noise ratio (SNR) of the received RF signal.

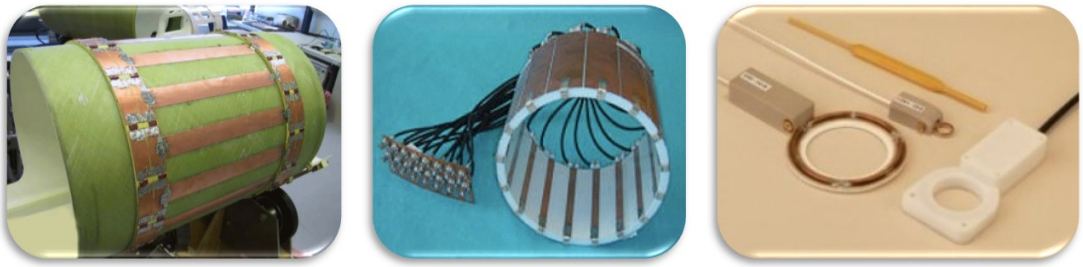

Figure 1.1: (a): A conventional high-pass birdcage coil, (b): a multichannel TEM array, (c): surface coils for RF reception. (Images are not subject to cophyright.)

For the MRI systems with low $\boldsymbol{B_0}$ strength ($< 3T$) and hence, low Larmor frequency ($f_0 < 127MHz$), birdcage coils are the preferred ones as they

can produce a highly homogeneous transmit field. Furthermore, the use of circuit theory techniques provide straightforward algorithmic design equations, facilitating their design and implementation processes [2].

For high and ultra-high field MRI systems, the most commonly used RF coils are TEM coils. Since they don't incorporate the end rings, and designed with the RF design techniques, they tend to give more homogeneous transmit fields at higher fields. On the other hand, their geometrical structure can become highly complicated and there are no straightforward design equations for their design.

The two most widely used RF volume *coils*, having either a single port or two ports being located at geometrically 90° apart places allow the RF transmission/excitation to be either quadrature or linear. The linear drive, being used in single-port coils, requires the coil to be excited from the only port. On the other hand, the quadrature drive requires the coil to be excited with 90° phase difference between the geometrically 90° apart ports.

1.1.2 Multichannel RF Arrays

The concept of RF *array* is used to describe the volume coils having more than two ports being deliberately decoupled (isolated) from each other. The commonly used ones in this sense are the degenerative birdcage arrays such as in [3, 4] and multichannel TEM arrays such as [5]. Being very similar in structure, the TEM or birdcage *arrays* can be constructed by adding more ports to their *coil* versions and by decoupling the individual line elements.

The main objective of constructing a decoupled volume array is to perform $\boldsymbol{B_1}$ shimming (adjustment) inside the object to be imaged. By spatially adjusting the magnitude of B_1^+, one can increase the strength of excitation in a particular region, which results in higher SNR values. Furthermore, deliberate reduction of the excitation strength at particular regions is used to reduce the specific absorption rate (SAR) at those locations.

1.2 Electrical Tissue Mapping and Electrical Properties Tomography (EPT)

Electrical tissue properties (EP's), namely, electrical conductivity (σ) and permittivity (ϵ), provide important clinical information about cancerous tissues as well as being useful in distinguishing between ischemic and hemorrhagic stroke [6–8]. They are also important in finding the specific absorption rate (SAR) in tissues during magnetic resonance imaging (MRI) scans and also in inverse problems of electrophysiology [9, 10].

In general, EP's are frequency dependent [11]. Previous techniques, aiming at imaging tissue properties such as electrical impedance tomography (EIT) [12], magnetic resonance electrical impedance tomography (MR-EIT) [13, 14] and magnetic induction tomography (MIT) [15] reconstruct the tissue properties at frequencies mostly lower than 100 kHz. A more recent technique, magnetic resonance - electrical properties tomography (MR-EPT) makes use of MRI technology and aims at reconstructing tissue properties at radio frequencies.

1.2.1 A Review on MR-EPT Studies

MR-EPT studies generally use the clockwise - circularly polarized components of the high frequency magnetic field of MRI, denoted by H^+, where $H^+ = B_1^+/\mu_0$. In terms of the applied methods (integral or derivative based), these studies provide either pointwise (local) or global EP reconstructions [16]. In pointwise EP reconstructions [17–19], including the Helmholtz's equation based standard (conventional) MR-EPT [17], the EP reconstruction on a certain pixel is only affected by the H^+ data on itself and by the H^+ data on nearby pixels. This is due to the application of Laplacian operator and some filter kernels during EP reconstruction [16]. Formulation of electrical conductivity (σ) and relative permittivity (ϵ_r) reconstructions in the standard MR-EPT are given as in the

following [17]:

$$\sigma = Re\Big\{\frac{\nabla^2 H^+}{i\omega\mu_0 H^+}\Big\}, \qquad \epsilon_r = Im\Big\{\frac{\nabla^2 H^+}{i\omega^2\epsilon_0\mu_0 H^+}\Big\} \tag{1.2}$$

where $\omega = 2\pi f_0$, f_0 is the Larmor frequency and μ_0 is the permeability of free space.

On the other hand, global studies such as convection-reaction equation based MR-EPT (cr-MREPT) [20, 21], gradient-based MR-EPT (g-EPT) [22] and contrast source inversion EPT (CSI- EPT) [23] reconstruct the EP's by solving the EPT equations over the entire region of interest. In these studies, each pixel/voxel of the reconstructed EP's are affected (constrained) by the inter-voxel relations and hence, they tend to be less prone to noise contamination.

Another criterion used in comparing MR-EPT algorithms is whether they make the assumption of homogeneous EP distribution in the region of interest (ROI). Algorithms described in [17, 18] assume that the EP's are slowly varying over the ROI, and they give inaccurate reconstructions at tissue boundaries where EP's may drastically vary [16]. On the other hand, methods described in [20–23], including cr-MREPT, do not make the assumption of homogeneous EP distributions and therefore the EP's at the tissue boundaries are better reconstructed.

Regarding the global studies, the CSI-EPT method is based on the constrained minimization of a cost function which is norm of the difference between measured and calculated B_1^+ distributions. The calculated B_1^+ is found by solving a forward model of the MRI coil system and the object, which relates B_1^+ to the electrical properties of the object. Although this method is robust against noise, it is computationally demanding since it requires the handling of the problem in a 3-D setting as well as an accurate model of the MRI system. A similar method, global maxwell tomography (GMT), which is based on integral equations, solely makes use of the B_1^+ field magnitude and it has only been tested with numerical simulation phantoms [24]. The g-EPT method, calculating the derivatives of the absolute and relative transmit B_1^+ phases works very well for ultra-high fields

($\geq 7T$), however, the technique requires too many experiments with different transmit-receive configurations from various channels of a multitransmit array for reconstructing the relative and absolute phases of the B_1^+ field. Another variant of the global algorithms described in [25] and [26] make local homogeneity assumption in their forward problem formulations (e.g. they use the formulation $\nabla^2\phi^+ = w\mu_0\sigma$ to calculate ϕ^+ (phase of B_1^+) from a given distribution), but solve the inverse problem in the global sense by fitting measured data to the calculated data. Nevertheless, they need to make heavy use of regularization techniques to constrain their solutions for not having excess variations near the boundaries. Finally, the cr-MREPT method can reconstruct EP's with a single experiment, however, it uses the transceive phase approximation (TPA) [27] for acquiring the phase of the B_1^+ field.

For the g-EPT method, in regions where $\frac{\partial H^+}{\partial x} - i\frac{\partial H^+}{\partial y}$ has low magnitude, a global bias in the EP reconstructions is observed [16]. Likewise for the cr-MREPT method, a spot-like artifact arises in such regions [20, 28]. In cr-MREPT studies, $\left[\frac{\partial H^+}{\partial x} - i\frac{\partial H^+}{\partial y},\ \ i(\frac{\partial H^+}{\partial x} - i\frac{\partial H^+}{\partial y})\right]^T$ is referred to as the "convective field" and the spot-like artifact is called the low convective field (LCF) artifact. In particular, EP reconstructions attain significantly incorrect values (generally abruptly occurring peaks or dips) at the regions of LCF artifact [20]. More importantly, the EP reconstruction performance of the cr-MREPT algorithm is significantly reduced where a tissue boundary coincides with an LCF region and this means that the main advantage of the cr-MREPT algorithm is severely distorted.

In order to alleviate the obstructions, brought forth by the low convective fields, methods that are altering the B_1^+ distribution are proposed. One of these methods developed in [29] uses materials with high dielectric constants for padding around the object and aims at altering the B_1^+ magnitude distribution within the object. With wisely located dielectric pads, spatial shift of the LCF regions is accomplished and as a result, the locations of the LCF artifacts are also shifted. Finally, two set of equations utilizing the B_1^+ distributions with and without padding are simultaneously solved to obtain an artifact-free reconstruction [29].

Another study, working on reducing the LCF-related artifacts, was presented in [30, 31] and solves the B_1^- based cr-MREPT equation ($B_1^- = \mu_0(H_x - iH_y)^*/2$), merging the data from different channels of a multi-receive coil. When a four channel phased array type receive head coil is used, the LCF regions for all channels overlap in the middle of the object. Therefore, it is not possible to eliminate central LCF artifacts, although the method is successful in non-central ROIs.

1.2.2 B_1 Magnitude and Phase Retrieval

The MR-EPT studies mentioned in the previous chapters use the complex transmit field (B_1^+). Retrieval of the complex B_1^+ is traditionally accomplished by acquiring its magnitude and phase in different steps. While there exists conventionally settled methods for obtaining the magnitude of B_1^+ for both quadrature and non-quadrature excitation [32], there is no straightforward method to obtain the *absolute* phase of the transmit field. Although there are studies to calculate the derivatives of the transmit phases, which can also be used to determine the electrical property maps [22, 33, 34], a conventional method to estimate the *absolute* transmit phase is still the subject of many inquiries.

One of the most common methods for gathering the phase of the transmit field is the transceive phase approximation (TPA) which assumes that the transmit and receive phase distributions of the transceiver coil are equivalent and therefore half of the acquired *transceive phase* is used as the transmit phase [18, 27]. TPA works best for the cases of quadrature excitation and quadrature reception with a birdcage or transverse electromagnetic (TEM) coil, when the static magnetic field strength is lower than or equal to $3T$ [18, 27]. For the cases of non - quadrature excitation, however, TPA fails [33, 35] and there are different methods to estimate the absolute transmit phase such as in [36]. The study [36], which is based on polynomial approximation of the B_1^+ phase, local homogeneity of the electrical properties is assumed and phase estimation near boundaries can be less reliable [16]. On the other hand, in the methods [22, 33, 34], the spatial derivatives of the

absolute transmit phase are estimated and the absolute phase can be derived by integration, starting from a seed point. However, these methods require many transmit-receive experiments and are computationally demanding.

1.3 Focus and Flow of the Thesis

This thesis, as a continuation and enhancement for the cr-MREPT method, focuses on the elimination of the LCF artifact from the conductivity and permittivity reconstructions. Implementation of the proposed method involves B_1 shimming operations with a multichannel TEM array. In this regard, the overall thesis includes three significant steps:

- Design, implementation and construction of the eight channel TEM array,
- Simulation based design of the artifact elimination algorithm,
- Practical implementation of the algorithm with the TEM array.

Design of this array was initiated by carefully scrutinizing the original TEM resonator structure in chapter (2). Deeply understanding the circularly polarized transmit and receive fields (B_1^+ and B_1^{-*}), a less sophisticated microstrip transmission line based eight – channel TEM array was designed and simulated in chapter (3). Use of the constructed array for MRI image acquisition is thoroughly explained in chapter (4).

The artifact elimination algorithm, being published in [37] with the name "Optimal Multichannel Transmission for Improved cr-MREPT" is given in chapter (5). This method uses two RF excitations for artifact reduction. In the first drive (quadrature drive), the conventional birdcage-like volume coil excitation is applied where B_1^+ magnitude exhibits the usual "central brightening" behavior and the LCF region occurs roughly at the center of the object. In the second drive (modified drive), the B_1^+ magnitude at the center of the object is

varied by applying optimized input RF sinusoids to the input ports of the TEM array. This B_1^+ magnitude variation shifts the LCF region away from the center such that the LCF regions in normal and modified drive experiments do not overlap. Finally, B_1^+ distributions from these two drive cases are simultaneously used to converge on a single artifact-free EP reconstruction.

Chapter (6) focuses on the practical implementation of the proposed method. Regarding the issues on B_1^+ phase retrieval, we propose another novel method to retrieve the transmit phase in the non-quadrature drive experiments. In that method, estimation of the non-quadrature drive transmit phase involves an additional quadrature drive experiment in which the receive phases of each channel are found with TPA assumtion. Then, these receive phases are used to obtain the transmit phase of the quadrature drive, from the MR-wise measurable transceive phase.

With the use of the artifact elimination algorithm, multichannel TEM array and the transmit phase retrieval method, thesis is concluded with the primary experimental conductivity reconstructions.

Chapter 2

Transverse Electromagnetic (TEM) Resonator

The idea governing the necessity of a transmission line based transverse electromagnetic (TEM) resonator was first recognized by Schneider and Dullenkopf in 1976. Later, Röschmann came up with his own solution to the electric field loss problems by designing a slotted "tube" of half wave coaxial transmission lines. Finally, the idea was reframed by J. Thomas Vaughan to allow variable tuning option to the coaxial transmission line based TEM resonator by introducing a variable - size air gap in the middle of each coaxial transmission line element.

2.1 Theory

In its very basic terms, the TEM *resonator* is a cylindrical re-entrant cavity resonator, being similar to the ones used in klystrons and microwave triodes [1]. This reentrant cavity, being shown in figure (2.2) is designed to resonate at a desired frequency, which needs to be the Larmor frequency corresponding to the particular MRI system, i.e. 127 MHz for 3 T scanners.

To understand this model approximation and the resonant frequencies of this structure, therefore, transmission line theory will be covered in its very basic terms.

2.1.1 Basics of Transmission Line Theory

The structure, being invented by J. Thomas Vaughan uses both open-circuited and short-circuited transmission lines. For understanding the resonant frequencies of these open and short ended transmission lines, the analytical formulations of input impedance for open and short circuited coaxial lines will be discussed.

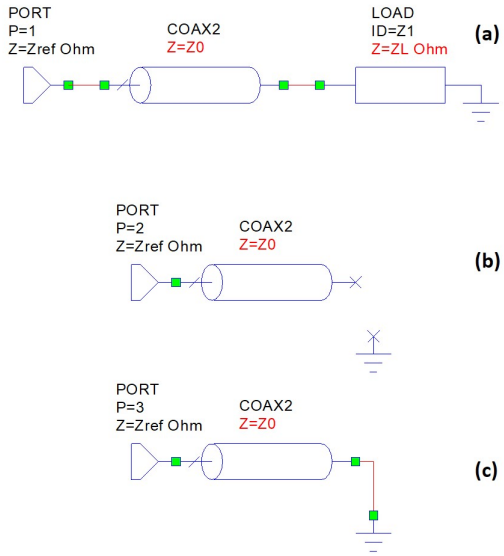

Figure 2.1: (a): A conventional coaxial transmission line of Z_0, terminated with a load impedance of Z_L, (b): Open ended transmission line, (c): A shorted coaxial transmission line.

The input impedance, seen from Port (1) in figure (2.1 (a)) is the ratio between voltage and current at $z = 0$ plane and given by the following [38]:

$$Z_{in} = V_{z=0}/I_{z=0} = \frac{V_0^+ e^{-\gamma z} + V_0^- e^{\gamma z}}{I_0^+ e^{-\gamma z} + I_0^- e^{\gamma z}} \tag{2.1}$$

where V_0^+ and I_0^+ are the forward travelling voltage and current, V_0^- and I_0^- are the backward travelling voltage and current, and γ is the complex sum of attenuation constant α (in $Neper/m$) and propagation constant $\beta = 2\pi/\lambda$ (in rad/m) such that $\gamma = \alpha + i\beta$.

For a transmission line with characteristic impedance Z_0 and length l, equation (2.1) can also be written in terms of Z_0 and load impedance (Z_L) as in the following [38]:

$$Z_{in} = Z_0 \frac{(Z_L/Z_0) + \tanh(\gamma l)}{1 + (Z_L/Z_0)\tanh(\gamma l)} \tag{2.2}$$

As the transmission line is open - circuited ($Z_L \to \infty$), as in figure (2.1(b)), the input impedance can be written as [38]:

$$Z_{in} = Z_0 \coth(\gamma l) \tag{2.3}$$

For a short circuited transmission line ($Z_L = 0$) as given in figure (2.1(c)), the input impedance seen from Port (1) can be derived as [38]:

$$Z_{in} = Z_0 \tanh(\gamma l) \tag{2.4}$$

Now, approximating equation (2.4) with the standard identities as in the following equation,

$$Z_{in} = Z_0 \frac{\sinh(2\alpha l) + i\sin(2\beta l)}{\cosh(2\alpha l) + \cos(2\beta l)} \tag{2.5}$$

where Z_0 is purely real, the input impedance seen by port (1) will be purely real for the frequencies where $\beta l = n\pi/2$ (where n is an integer). Therefore, the resonance frequency of a short circuited transmission line is given as in the following [1]:

$$f_r = \frac{nV_p}{4l} \tag{2.6}$$

where $V_p = c/\sqrt{\epsilon_r}$ is the phase velocity of the travelling wave inside the coaxial transmission line, being filled with a material with relative dielectric constant as ϵ_r (it should be noted that the relative permeability is always assumed to be equal to 1).

If the coaxial line is a low loss line, the phase velocity can be approximated in terms of the inductance and capacitance as $V_p \approx 1/\sqrt{LC}$ and therefore, the resonant frequency will be approximated by $f_r = \frac{n}{4l\sqrt{LC}}$.

2.1.2 The Re-Entrant Cavity Resonator

As it was briefly mentioned before, the idea behind the original TEM coil was to design it as a cylindrical re-entrant cavity resonator which is shown as in figure (2.2)

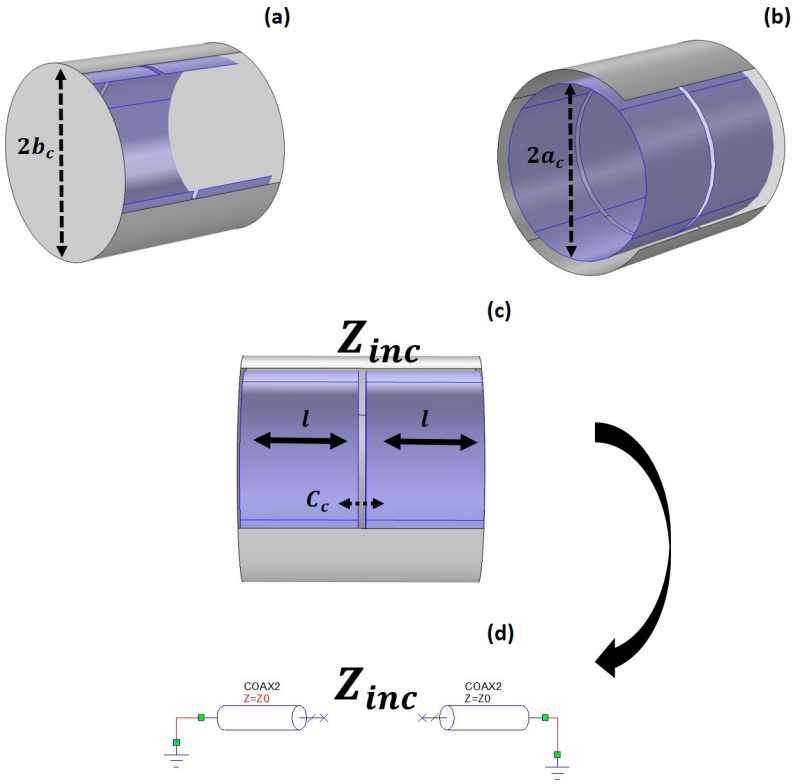

Figure 2.2: The re-entrant cavity resonator shown in three perspective angles for better visualization. All of the walls of the cavity resonator are supposed to be perfect conductors and the inner conductor is bisected in the middle. It should be noticed that Z_{inc} corresponds to the resultant input impedance due to the both ends of bisection.

The reentrant cavity resonator, having an outer radius of $2b_c$, inner radius of $2a_c$ and a length of nearly $2l$ (neglecting the gap in the middle) can also be modeled as a bisected coaxial transmission line shorted at both ends, as shown in figure (2.2 (d)).

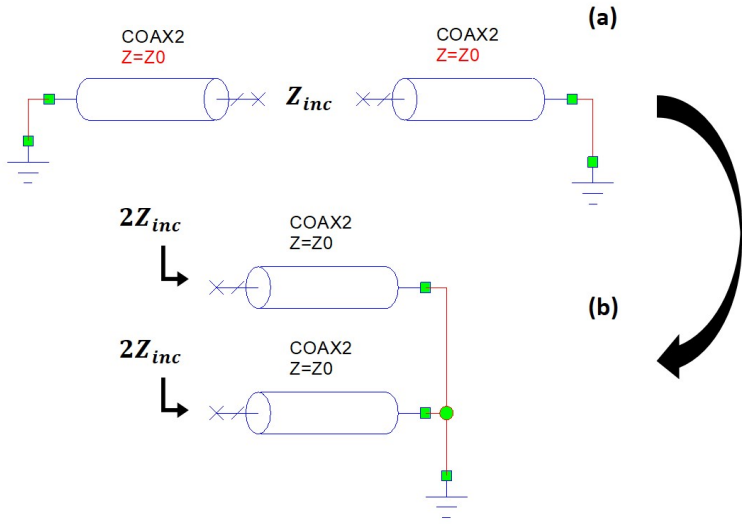

Figure 2.3: (a): Model approximation of the cavity resonator as two shorted coaxial transmission lines, (b): Equivalent circuit of (a). It should be noted that the Z_{inc} is the total (resultant) impedance seen in the middle, due to the both sides of the resonator.

The approximation model of the re-entrant cavity shown in figure (2.2 (d)) characterizes it as a coaxial transmission line being shorted at both ends and bisected by a gap capacitance in the middle. This approximation model, used in [1] serves as a backbone in the design of the dimensions of the coil according to a desired resonant frequency.

The overall input impedance, which actually takes into account both sides of the resonator is denoted as "Z_{inc}" in figure (2.1). The frequency at which Z_{inc} is purely real correspond to the resonant frequency of the re-entrant cavity. This particular frequency can be estimated in terms of transmission line equations given in the previous section. However, as we introduce new coaxial transmission lines inside the cavity resonator –which will be described in the following sections–, this approximation will fail to estimate the overall resonant frequency and therefore, corresponding distributed impedance coefficients of this cavity (L_c, C_c) will be required. Determination of these coefficients are based on different approximations, as given in [1] and will not be fully discussed in too much detail.

The impedance "Z_{inc}" of the re-entrant cavity, shown in figure (2.1) is revisited in figure (2.3) and as shown, it is modelled as the input impedance of a parallel connection of two equivalent short circuited transmission lines.

Therefore, when $2Z_{inc} = \omega L_c$ and also $2Z_{inc} = 1/(\omega C_c)$ are considered, the distributed inductance and capacitance can be found in terms of the input impedance Z_{inc}. This input impedance can also be found from equation (2.4) and when these quantities are equated, L_c and C_c can be found as:

$$\begin{aligned} L_c &= 2Z_{0c}\tan(\beta l)/\omega, \\ C_c &= 1/(2\omega Z_{0c} tan(\beta l)) \end{aligned} \tag{2.7}$$

In equation (2.7), the characteristic impedance of the re-entrant cavity, being denoted by Z_{0c} is found by the standard empirical formula for a coaxial transmission line and given as: $Z_{0c} = (\eta/2\pi \ln(b_c/a_c))$ where η is the wave impedance such that $\eta = \sqrt{\mu/\epsilon}$ [38].

Hence, the resonance frequency of the re-entrant cavity can be written in terms of the distributed impedance parameters as:

$$f_{res} = \frac{1}{2\pi\sqrt{L_c C_c}} \tag{2.8}$$

The re-entrant cavity which has been described so far obviously cannot be considered as a coil for NMR applications. Transformation of this structure into a TEM wave supporting apparatus will be addressed in the subsequent sections.

2.2 Coaxial Line Element Based TEM Coil

As described in the previous sections, the re-entrant cavity resonator is not yet a TEM coil. In order for flipping the longitudinally directed magnetization vectors in a biological tissue to be imaged via an MRI scanner, we need TEM wave

propagation ($E_z = H_z = 0$) inside the utility center of the resonator. This requirement on the other hand, necessitates the conducting walls of the re-entrant cavity to be slotted.

A re-entrant resonator with slotted inner conductor wall can be seen in figure (2.4(a)). In [1] on the other hand, it has been stated that leaving the slotted inner wall of the coil like that will yield the electric field to "leak" around its vicinity, yielding obstructions on matching and tuning. Therefore, the floating outer conductors shown in (2.4(b)) were introduced to conserve the electric field largely within the dielectric regions between the inner and outer conductors. Therefore, the TEM wave is expected to be stored within the "coaxial line elements" of the coil. It should be noted that the "floating" outer conductors are not touching either to the outer conductor wall (shield) or to the inner conductors of the coil. Furthermore, the center (inner) conductors of the coaxial line elements are connected to the outer wall of the coil in both ends. In figure (2.4), the purple boundaries demonstrate the perfect electric conductor layers of the coaxial element based TEM resonator.

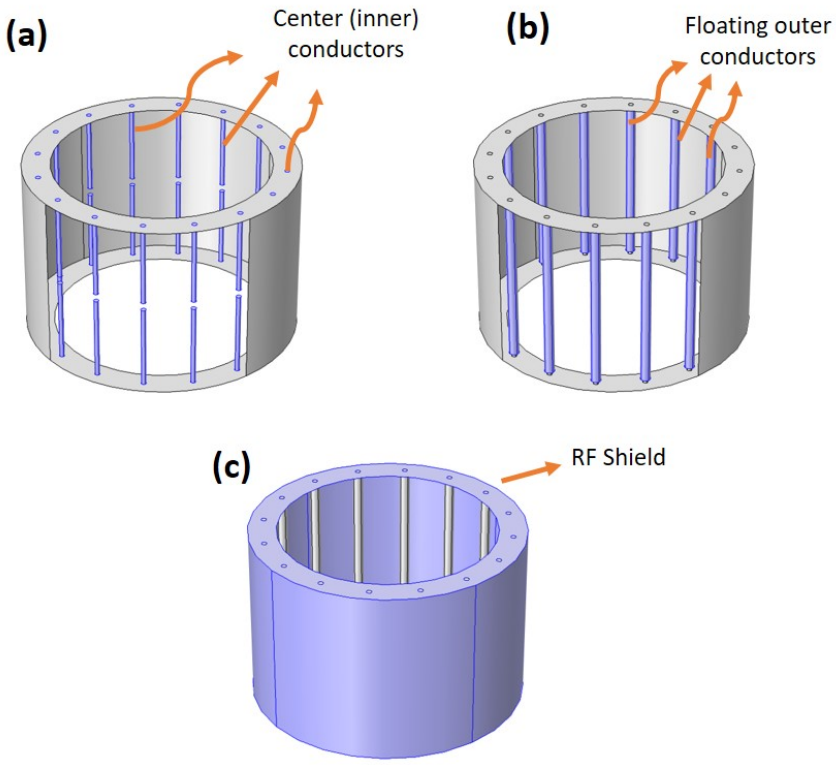

Figure 2.4: Constructed CAD model of the 16 element TEM resonator being designed and implemented in [1]. The purple boundaries correspond to the perfect electric conductors. (a): The inner conductors of the coaxial line elements, (b): Floating outer conductors, (c): The RF shield, serving as the ground plane.

In order for this structure to work properly, both the line elements and the re-entrant cavity need to resonate in tandem. On the other hand, addition of the coaxial line elements inside the re-entrant cavity leads these line elements to produce inductively coupled resonating modes, hence, making the ongoing electromagnetic phenomena inside the coil even more difficult to understand. It is obvious that the derivation of accurate analytical solutions for the resonant modes of such a convoluted structure is horrendously challenging. In this regard, many different numerical models have been proposed just in order to estimate the resonating modes of this structure such as in [39].

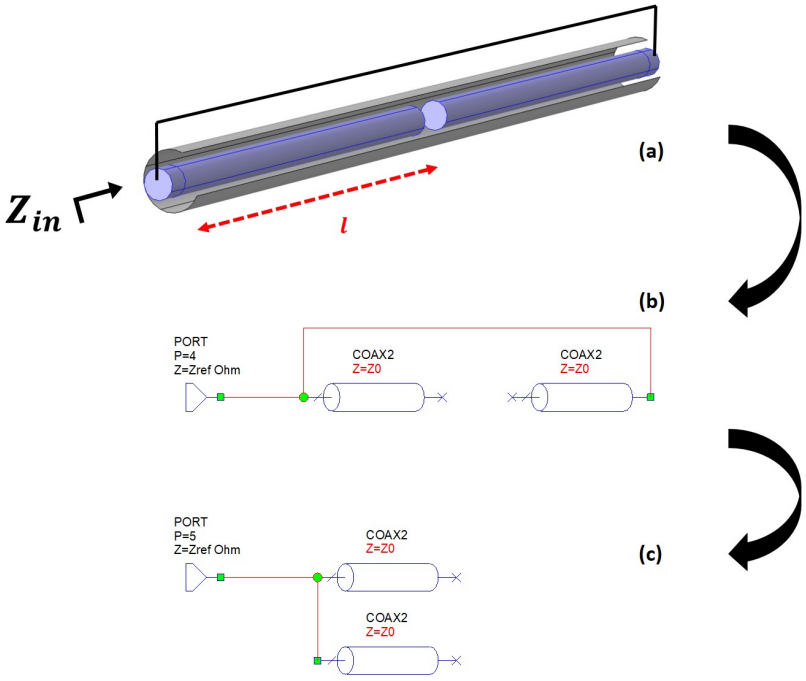

Figure 2.5: A single line element of the coil. (a): The coaxial line element, (b,c): approximation models of the line element.

A very simple model to characterize the coil in order for the designers to better comprehend the electromagnetic structure was provided by the inventor of the coil in [1]. To estimate the frequency at which the overall structure resonates, it was suggested to calculate the resonant frequency of the re-entrant cavity and a single line element separately – by finding their approximate inductance and capacitance values – and then to combine these resonant frequencies.

In order to find the frequency at which a single line element resonates, each single one is considered as two separate coaxial transmission lines being connected at the input, as shown in figure (2.5). This is a valid approximation as the outer conductive wall of the coil (shield) actually connects the inner conductors of the line elements. In this regard, the single line element is simplified to the model in figure (2.5(c)), which characterizes it as two open circuited coaxial transmission lines connected at the input port. In this case, estimating the distributed element coefficients C_e and L_e will be accomplished in a very straightforward manner, in

terms of the input impedance (Z_{in}) shown in figure (2.5).

$$\begin{aligned} C_e = 1/(2\omega Z_{in}) \approx l/(2Z_{0_e}V_p), \\ L_e = 2Z_{in}/\omega \approx Z_{0_e}2l/V_p \end{aligned} \tag{2.9}$$

In equation (2.9), Z_{in} can be calculated from equation (2.3) and the characteristic impedance of a single line element is $Z_{0e} = (\eta/2\pi \ln(b_e/a_e))$ where b_e and a_e are the outer and inner radii of the line elements and η is the wave impedance inside the medium between inner and outer conductors such that $\eta = \sqrt{\mu/\epsilon}$. It should be noted that $\epsilon = \epsilon_r\epsilon_0$ and $\mu = \mu_0$ are the permittivity and the permeability of the dielectric material between the inner and outer conductors.

To this end, the resonance frequency of both the reentrant cavity and the line elements are separately estimated. Obtaining the frequency at which the overall structure resonates, the total series inductance L_t and capacitance C_t values need to be calculated with the following equations:

$$\begin{aligned} L_t \approx L_c + L_e/N, \\ C_t \approx NC_e \end{aligned} \tag{2.10}$$

Equation (2.10) finalizes the model for estimating the overall resonance frequency of the TEM coil described in [1]. However, since the coil incorporates the line elements located in close vicinity of each other, the RF currents running on these transmission lines perform an inductive coupling effect in each other, resulting in more than a single resonance frequency. These different frequencies at which the structure resonates, generate different $B_1^+ = \mu_0 H^+$ field distributions (modes) within the utility center of the coil.

The model given above is a very crude approximation of the resonance frequency and does not take into account the inductive coupling of the line elements. Although it gives an insight on the electromagnetic working principle of the TEM coil, it was also stated in [1] that the actual design of this system

can only be made with numerical simulations.

Therefore, we used finite element method (FEM) based techniques in the "RF Module" Comsol Multiphysics (Comsol A B, Sweden) to simulate the structure, which will be discussed in the subsequent sections.

2.2.1 Inductively Coupled Modes of the TEM Coil

As stated in the previous section, the TEM coil incorporating the line elements have different inductively coupled modes (B_1^+ field configurations). According to [1], an N element coil produces $(N/2+1)$ modes. In the $M'th$ mode, the phase difference between the RF currents running on two adjacent line elements are given as $\phi_M = 2\pi M/N$.

In order to find these modes of the TEM coil, the structure is analyzed with the eigenfrequency analysis of the RF Module of Comsol Multiphysics. Figure (2.4) depicts the structure in the Comsol design environment.

The eigenfrequency analysis was performed around 175 MHz, as this is the frequency at which this coil was designed to resonate. The B_1^+ field distributions and surface current densities ($\boldsymbol{J_z}$) on the inner conductor of the coil are demonstrated in figure (2.6). As it can be seen, the $\boldsymbol{J_z}$ distribution of "Mode 0" – the cyclotron mode – of the resonator shows that all of the currents have the same magnitude and same phase. This cyclotron mode is not suitable for clinical NMR applications as each two line element, being symmetrically located with respect to the center of the coil will produce destructively interfering B_1^+ fields and therefore, as it can be seen from figure (2.6), the value of B_1^+ magnitude is nearly zero inside the coil.

The first mode, "Mode 1" of the resonator, however, demonstrates a linearly increasing RF current phase offset from line element 1 to 16. This mode, having $\pi/8$ radians of current phase increments among the adjacent line elements, generates a nearly homogeneous B_1^+ magnitude distribution at the interior region

of the coil and is used for the clinical NMR applications [1]. The B_1^+ field and $\boldsymbol{J_z}$ distributions for the third and fourth modes of the TEM resonator are also depicted in figure (2.1).

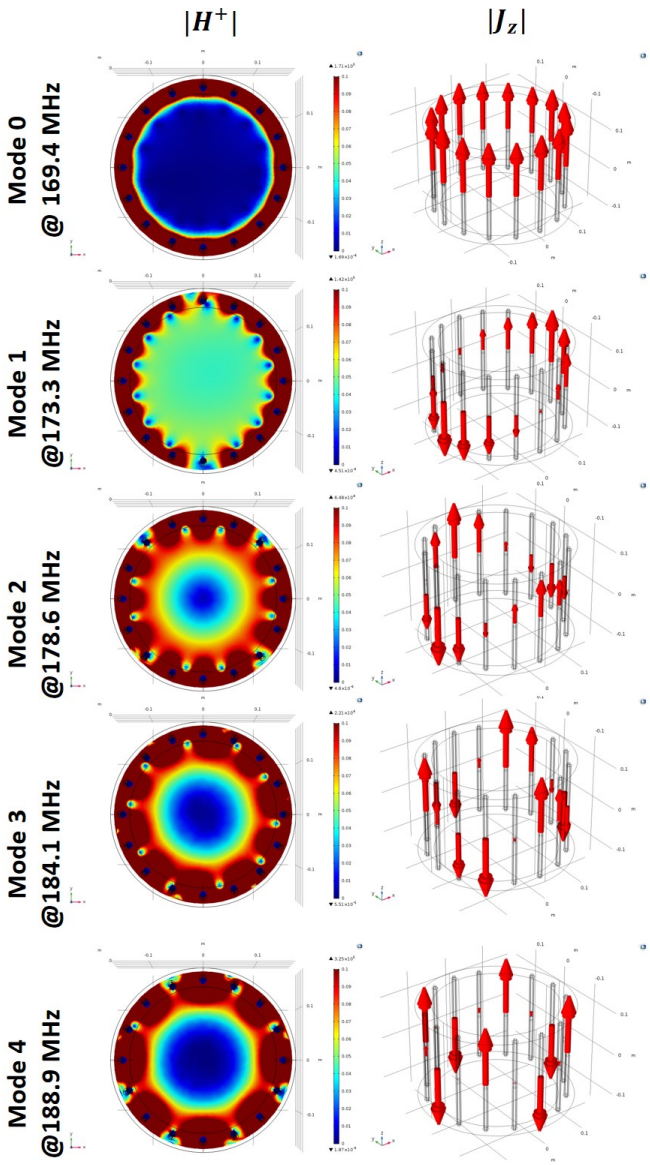

Figure 2.6: TEM resonator B_1^+ magnitudes according to the coupled modes of the array.

Mode 1 of the TEM resonator has the most commonly used B_1^+ distribution in clinical studies. This inductively coupled mode is also very similar to the rotating

field generated by a birdcage coil, which is commonly used in MRI systems with static field strengths lower than or equal to $3T$. In this mode, the $\boldsymbol{H}$ field is directed towards a single direction and therefore, it is polarized. According to the driving configuration (either quadrature or linear drive), the polarization of the $\boldsymbol{H}$ field becomes either circularly or linearly polarized. This issue will be examined in more detail in the following sections.

The generated $\boldsymbol{H}$ field, which can be seen in figure (2.7) only has transverse (x and y) components and no z component as the wave travelling inside the coil is a TEM wave.

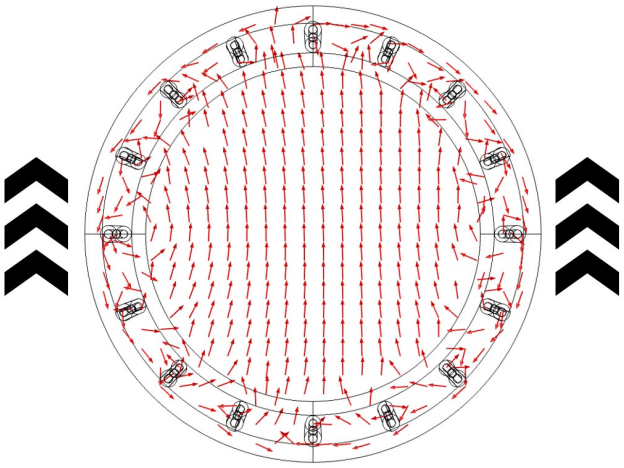

Figure 2.7: $\boldsymbol{H}$ field of Mode 1 of the TEM array. As it can be seen, it is pointed toward upwards.

Understanding the internally generated field and the geometrical structure of this TEM resonator, we proceeded by adjusting the resonance frequency to 123.2 MHz, which is the Larmor Frequency of 3 T (nominal value, real value turns out to be 2.89 T) MRI systems. In this regard, the coarse frequency tuning is made by altering the length of the line elements (coaxial transmission lines) while the fine tuning was achieved by spatially shifting the inner conductors of the coaxial transmission lines inside the dielectric pieces. This spatial shift acts by changing the capacitance (C_c) in the middle of the resonator. Furthermore, the number of line elements was lowered to 8 in order for feasible practical construction. The 8-leg TEM resonator, being designed for 3T MRI systems is explained in the

following section.

2.3 TEM Coil For 3T

Adjusting the first mode frequency of the TEM resonator to 123.2 MHz, and lowering the number of the line elements to 8, the new dimensions of the coil are given as: Height: 32.45 cm, Outer radius (b_c): 15 cm, inner radius (a_c): 11.5 cm, line element inner radius:(a_e) 3.25 cm, line element outer radius (b_e): 6.25 cm.

Adaptation of the original coil in [1] to 123.2 MHz was accomplished by trial and error, with the heavy use of eigenfrequency analysis. Analytical calculations were not used, as not recommended in [1]. The coil for 3 T can be seen in figure (2.8).

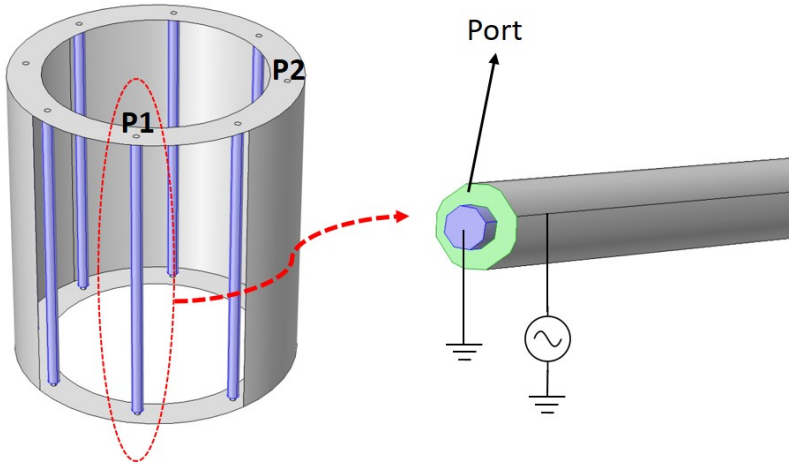

Figure 2.8: The coil for 3T and the driving port of the coil. The lumped port corresponds to the dielectric region between the inner and outer conductors of the line element.

With the use of eigenfrequency analysis, Mode 0 appears roughly at 119 MHz, Mode 1 appears at 123.2 MHz and so on. The frequencies at which the higher order modes appear are not important and will not be given.

In order to obtain the B_1^+ field at Mode 1, the coil needs to be driven from

a user-defined port with RF current having 123.2 MHz frequency. This port is defined as the dielectric material between the inner and outer conductors of the TEM coil, as shown in figure (2.8). On the other hand, there is an important point in the driving configuration of this port. As it can be noticed, the inner conductors of the line elements are connected to the shield and hence, all of the inner conductors of the line elements are connected to each other. In this regard, the floating outer conductors of the line elements should be used as the RF signal lines. This actually makes sense as the outer conductors of the coil are the ones which radiate and generate the desired B_1^+ field within the coil. Therefore, the + terminal of the signal generator will be connected to the floating outer conductor and the ground terminal will be connected to the inner conductor of the line element.

Just like driving a quadrature birdcage coil, there are two different possible driving conditions for driving an inductively coupled TEM coil. The first driving configuration, "Linear Drive" uses a single port on the coil for excitation. In this drive configuration, the coil is excited with an RF input only from Port 1, shown in figure (2.8). In the linear drive, the generated clockwise circularly polarized field (B_1^+) is equal to the counter-clockwise circularly polarized field (B_1^-). Therefore, the $\boldsymbol{B_1}$ becomes linearly polarized.

The second driving configuration, "Quadrature Drive" on the other hand, uses a second port which is geometrically 90° away from the first port, just as shown in figure (2.8). Just as in a conventional birdcage coil, when two channels (ports) are 90° apart from each other, these ports become geometrically decoupled (isolated) and therefore, the RF power being inserted from the first port will not either go away from the second port or interfere with the signal coming from the second port. In this drive configuration, the first port is driven without a phase offset, however the second port is driven with -90 degree of phase offset in order for achieving a constructive B_1^+ interference inside the coil. In the quadrature drive, the same $\boldsymbol{B_1}$ field can be generated as in the linear drive, however its counter-clockwise circularly polarized component (B_1^-) vanishes and the only remaining field is B_1^+. The H^+, H^- and $\boldsymbol{H}$ field distributions of linear and quadrature drive are depicted in figure(2.9).

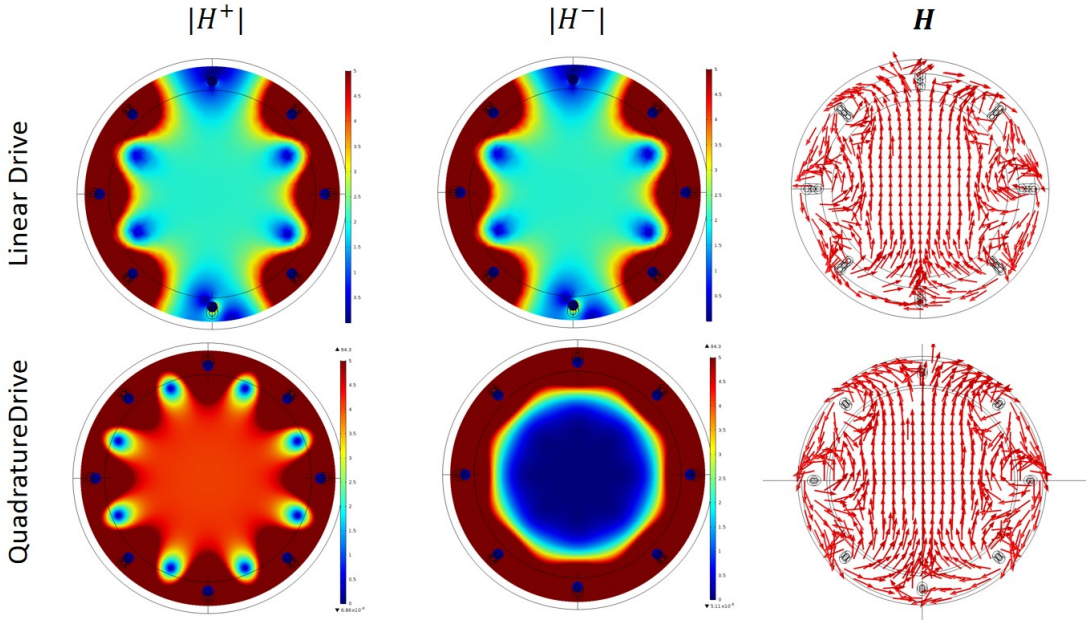

Figure 2.9: H^+ and H^- magnitude distributions of the empty coil in the cases of linear and quadrature drive configurations. $\boldsymbol{H}$ field distribution is also depicted in the figure with the directed arrows.

In figure (2.9) it should be noticed that the H^+ and H^- magnitude distributions of of the linear drive are equivalent. For the quadrature drive, as mentioned, the H^- distribution attains a value of zero at the center of the coil. On the other hand, it should be observed that the magnitude of H^+ distribution, generated by the quadrature excitation is nearly two times greater than that of the linear drive. This is a very important observation on the use of quadrature excitation in standard MRI coils. As the longitudinally directed spins of a biological tissue (to be imaged) is flipped by the transmit field (H^+) towards the transverse plane in MRI systems, the counter-clockwise polarized field (H^-) turns out to be insignificant during RF transmission. Since two times greater H^+ magnitude can be achieved with the quadrature excitation and this is the one that is most commonly used in conventional RF coils for MRI [2].

With the definition of ports and excitation configurations, a standart TEM coil, being compatible with the one used in [1] is modelled and simulated for a $3T$ MRI scanner. On the other hand, this coaxial-element based TEM coil turns out

to be highly challenging to construct and transforming this TEM "coil" into a TEM "array" will become horrendously difficult when more than two decoupled ports are desired. The design and simulations of this original TEM array serves as a departure point for our design and construction of the "Microstrip Line Element" based TEM array, which will be discussed in the following sections.

Chapter 3

Microstrip Based TEM Resonator

As discussed in the previous chapter, the simulations of the original TEM coil structure facilitated the understanding of the topology behind the RF transceiver coils for contemporary MRI systems. The design, published and patented by J. Thomas Vaughan turns out to be a novel and highly sophisticated approach on generating a circularly polarized transmit field (B_1^+) in a region. On the other hand, employing the principles of both transmission line and cavity resonators makes the design difficult to understand. Furthermore, straightforward design equations that can predict the frequencies of the coupled modes of that structure is an ongoing research topic.

Due to their less convoluted structure, "Microstrip Transmission Line (MTL) Based TEM Resonators" are much more ubiquitously used in high and ultra-high field MRI scanners. Even though these resonators work in a very similar working principle, absence of a resonating re-entrant cavity makes the MTL based resonators much more easy to design and construct. Furthermore, analytical models to predict the resonance frequencies turn out to be much more reliable.

In this chapter, the design and simulations of a MTL based TEM *coil* will

be given with an emphasis on the effect of design parameters on its practical implementation. After the design of this TEM *coil* with two input ports is given, it will be transformed into a TEM *array* having eight decoupled (isolated) ports. The designed and simulated TEM array will be used for RF shimming and MR-EPT studies in the subsequent chapters.

3.1 Theory

Departure point of the design of an MTL based coil is the design of the line elements, which are actual MTL resonators. In this regard, starting with the microstrip theory and some practical considerations will be convenient.

3.1.1 Microstrip Transmission Lines (MTL) and Resonators

Microstrip transmission lines are the most commonly used guiding structures due to their practical construction on printed circuit boards. A typical MTL drawing can be seen in figure (3.1). As the $\boldsymbol{E}$ and $\boldsymbol{H}$ fields of the propagating wave "leaks" outside of the dielectric material between the conductors, the MTL's are said to carry quasi-TEM waves rather than perfect TEM waves. Therefore, the characteristic impedance of the MTL's are calculated with an effective dielectric constant (ϵ_{eff}), rather than the relative dielectric constant (ϵ_r) of the material between the conductors. The effective dielectric can be calculated as in the following:

$$\epsilon_{eff} = \frac{\epsilon_r + 1}{2} + \frac{\epsilon_r - 1}{2}\left(\frac{1}{\sqrt{1 + 12(h/w_c)}}\right) \tag{3.1}$$

where h is the thickness of the dielectric material, w_c is the width of the upper conducting strip and ϵ_r is the relative dielectric constant of the material between the conductors. Using the effective dielectric constant, the approximated

characteristic impedance of a microstrip transmission line is given as:

$$Z_0 = \begin{cases} \frac{60}{\sqrt{\epsilon_{eff}}} \ln\left(8\frac{h}{w_c} + \frac{w_c}{4h}\right) & , w_c/h < 1 \\ 120\pi / \left(\sqrt{\epsilon_{eff}[w_c/h + 1.393 + \frac{2}{3}\ln(w_c/h + 1.444)]}\right) & , w_c/h > 1 \end{cases} \tag{3.2}$$

In clinical MRI coils, the characteristic impedance of MTL's are chosen between 20 and 120 Ohms in order for complying with the microstrip assumption. Charecteristic impedance values out of this range generally result in the propagation of waves having either $\boldsymbol{E}$ or $\boldsymbol{H}$ fields in the longitudinal direction, hence violating the TEM wave assumption [2].

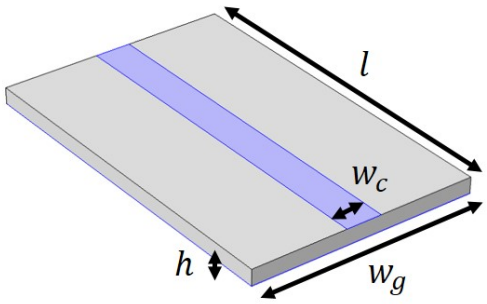

Figure 3.1: Drawing of a typical microstrip transmission line

3.1.2 MTL Resonators

As it was stated before, the line elements of the coil consist of microstrip resonators, being tuned to the Larmor frequency of the particular MRI scanner for which it is to be used. The most commonly used microstrip resonators in TEM coils are $\lambda/2$ open ended resonators. In some specific applications, when a longitudinally asymmetric B_1^+ field is required, $\lambda/4$ shorted resonators are preferred, however it does not serve for our purpose [2].

Designing microstrip lines of length $\lambda/2$ turns out to be highly impractical for the frequencies in which most MRI scanners operate. For instance, the RF wavelength is approximately 2.34 m for a $3T$ scanner ($f_0 = 127MHz$) which will require a transmission line of length 1.17 m. In order for shortening the wavelength inside the microstrip, using a material with high dielectric constant is an option. On the other hand, shunting the MTL at both ends with capacitors serves for the same purpose of wavelength shortening and is much more practical in terms of tuning the resonator to a desired frequency.

The behaviour of the actual $\lambda/2$ resonator and a both end shunted transmission line resonator is compared in figure (3.2) in terms of their input impedances. As it can be seen in the figure (3.2(a)), the $\lambda/2$ resonator "copies" the infinite load impedance (open circuit) to its input port by rotating the load impedance 360 degrees towards the input port. On the other hand, when there is no resistive loss, the shunt capacitors C_1 and C_2 move the load impedance on the purely imaginary circle defined by $Z = R + iX$, where $R = 0$ and therefore, a shorter transmission line can be used.

A sample microstrip transmission line, shunted at both ends with capacitors C_1 and C_2 can be seen in figure (3.2(b)). For getting a longitudinally symmetric B_1^+ field, the capacitance values of the capacitors need to be equivalent and calculated with the following equation [2]:

$$C_T = \frac{cos(\beta l) + 1}{\omega_0 Z_0 sin(\beta l)} \tag{3.3}$$

where l is the length of the MTL, $\beta = 2\pi/\lambda$ is the phase (propagation) constant, $\omega_0 = 2\pi f_0$ is the Larmor frequency and Z_0 is the characteristic impedance of the MTL. This equation can be derived by finding the frequency at which input impedance seen by Port 1 in figure (3.2(b)) is purely real.

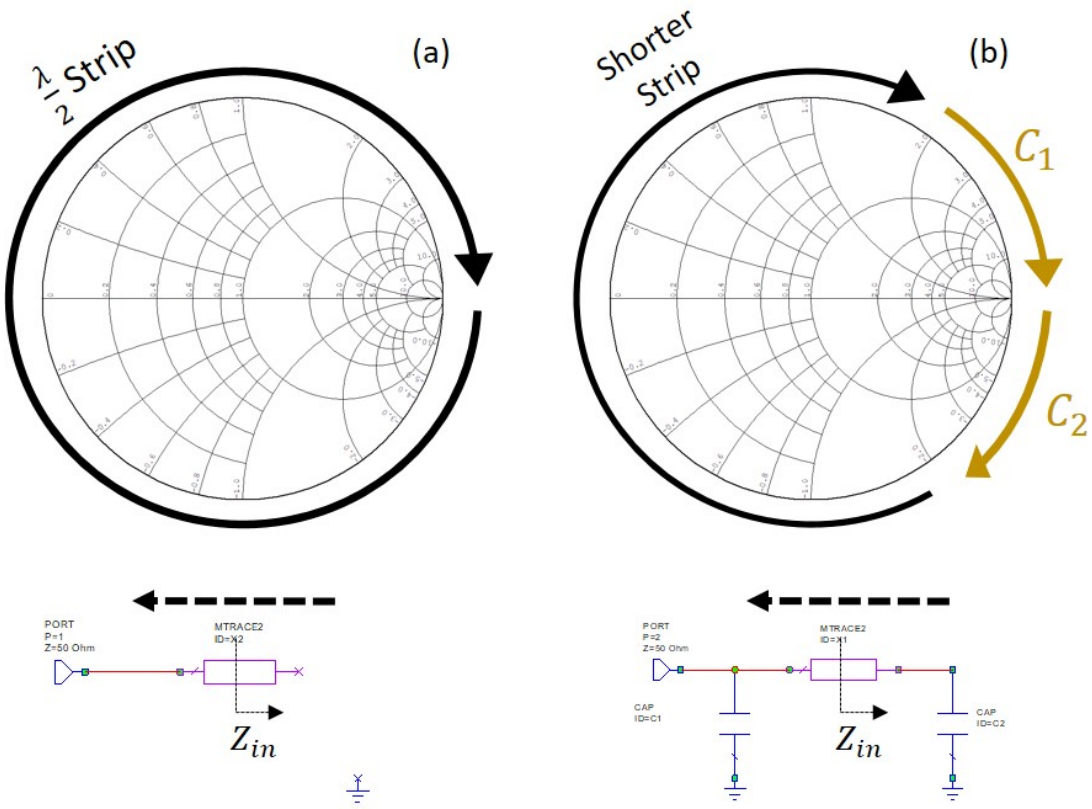

Figure 3.2: (a): Smith chart representation of the input impedance of a $\lambda/2$ open ended resonator and its schematic. (b): Smith chart representation of the input impedance of an MTL resonator shunted at both ends with capacitors C_1 and C_2 and its schematic.

With the design equations of both MTL's and the MTL resonators, the following sections explain the step-by-step design of the TEM coil and its transformation into a TEM array.

3.2 TEM Coil and TEM Array Design

Commencement with the design of a working TEM "coil" would be the initial step in terms of designing a TEM "array". The design flow of the TEM array is given as:

- Design of a TEM coil:

  Designing a single MTL resonator and tuning it to Larmor frequency,

  Forming the coil structure with eight of the designed equivalent line elements,

  Re-tuning the identical resonators to compensate for the frequency shift due to inductive coupling (Optional)

- Design of the TEM array:

  Decoupling of the inductively coupled line elements,

  Introducing loss and matching the input ports on the line elements.

The workflow summarizes the complete design of the TEM coil and its transformation into a TEM array. Therefore, each single step in the workflow will be addressed under different titles in the subsequent sections.

3.2.1 Tem Coil Design: Design of a Single Line Element

Design of the TEM coil departs from the design of a single line element, being an MTL resonator tuned to $123.2MHz$, which is the Larmor frequency of our MRI scanner with $3T$ nominal and $2.89T$ typical B_0 strength.

Characteristic impedance of the MTL's are chosen to be 50 Ω for easier matching and the length of the lines are chosen to be 30 cm. Plexiglass material (having $\epsilon_r = 3.6$) with 1 cm thickness is chosen for the dielectric material between the copper strips. With these pre-determined ones for feasible fabrication, the remaining parameters of the MTL's and the shunt capacitors are calculated with the design equations and optimized with the CAD tools such as AWR and Comsol Multiphysics. The capacitance values of the shunt capacitors and the MTL sizes are shown in table (3.1).

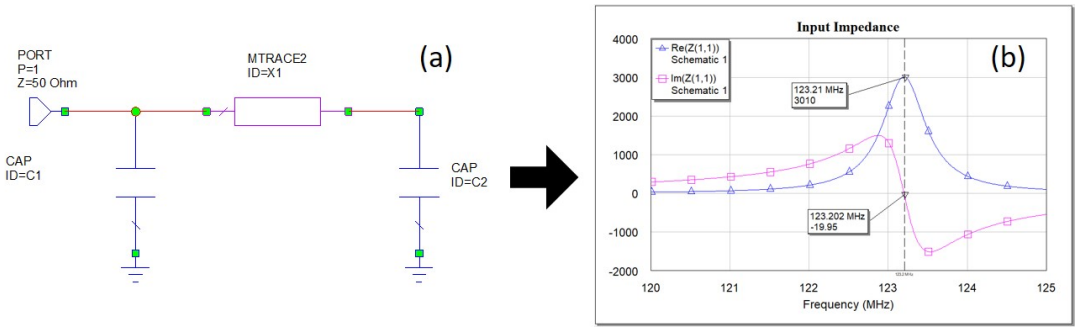

Figure 3.3: (a): Microstrip transmission line shorted at both ends to form a half wave resonator. (b): The real and imaginary parts of the input impedance of the shunted microstrip resonator.

ϵ_r	Z_0	w_s	h	w_g	l	C_t
3.6	54 Ω	2 cm	1 cm	12.56 cm	30 cm	34 pF

Table 3.1: Design parameters of a single line element, optimized in AWR.

The AWR simulations of a single line element with design parameters given in table (3.1) is depicted in figure (3.3). This line element, being shunted at both ends has the behavior of a typical $\lambda/2$ resonator. It should be noticed that the imaginary part of the input impedance of the resonator attains a value of zero at 123.2 MHz and its real part reaches a peak value at the same frequency.

3.2.2 Tem Coil Design: Coil Formation with the Line Elements

After a single line element of the TEM coil has been designed to resonate at the Larmor frequency, eight of these microstrip elements are merged to form an octagon shaped TEM coil. The octagon shaped TEM coil can be seen in figure (3.4). As it can be seen, the ground plates are also merged to act like an RF shield around the coil structure. This octagon-shaped TEM coil configuration is very similar to the coaxial element based coil, described in the previous sections, however, it does not have the resonating cavity, which makes it easier to understand.

In this octagon shape, the microstrip line elements will also perform an inductive coupling effect and the same inductively coupled resonating modes will arise. Just as in the coaxial based coil with eight elements, this structure generates $(8/2+1=5)$ different modes, hence, 5 different resonance frequencies. The mode that we are interested in is the first mode (the mode after the 0'th mode) in which there is 45 degrees phase difference between the running currents on the microstrip transmission lines. Due to inductive coupling, none of these modes have the resonant frequency at 123.2 MHz, which is the individual resonant frequency of a single line element.

In this configuration, the first mode of the TEM coil is detected at 122.665 MHz. When driven in the quadrature configuration from ports 1 and 2, the generated $|B_1^+|$, $|B_1^-|$ and $\boldsymbol{B_1}$ fields are depicted in figure (3.5). The surface current densities on the strips are also shown on the figure, revealing that the inductive coupling generates 45 degrees apart currents on the transmission lines. It should be noticed that the generated fields and currents are very similar to the coaxial element based coil.

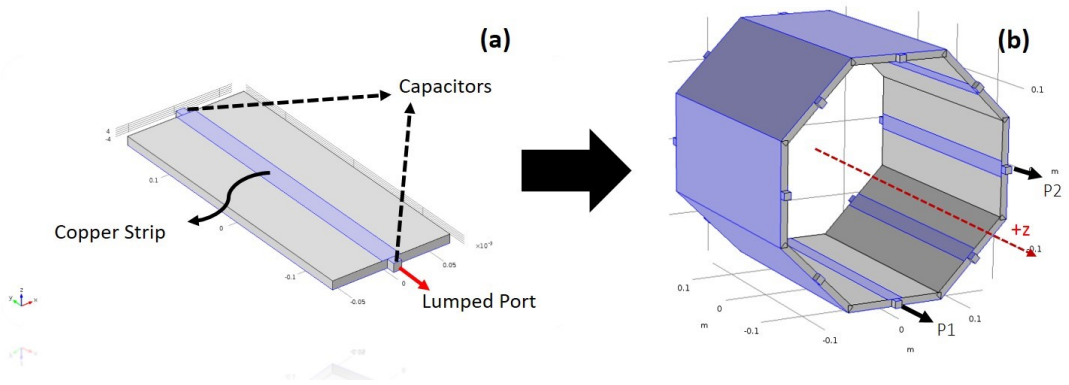

Figure 3.4: (a): Microstrip transmission line shorted at both ends to form a half wave resonator. (b): Eight line elements are merged to form an octagon shaped inductively coupled TEM coil.

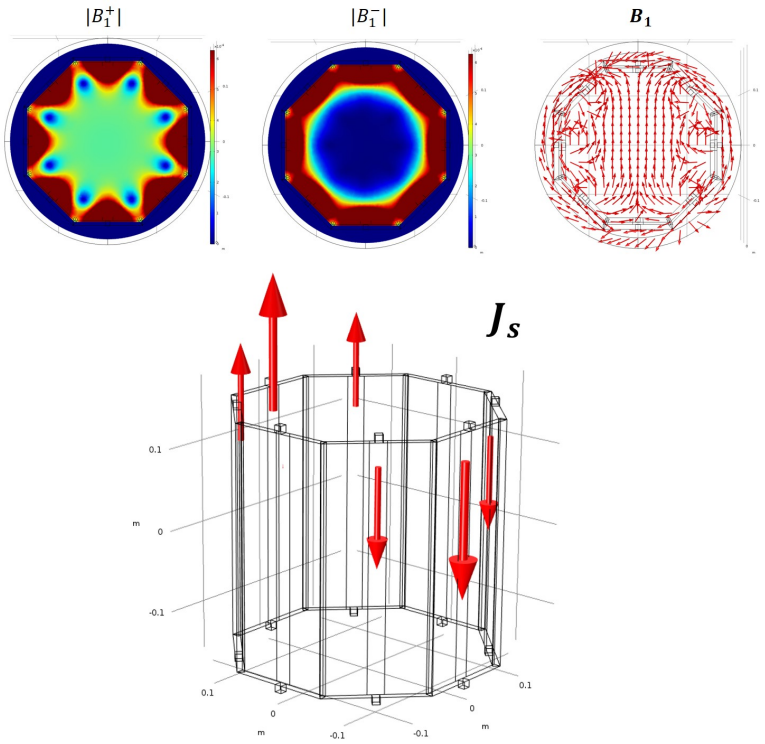

Figure 3.5: (a): The $\boldsymbol{B_1}$ fields of the MTL TEM coil and the surface current densities on the microstrips in quadrature excitation.

As the octagon shaped TEM coil structure is formed and the resonant frequency for the first mode is detected, either the lengths of the transmission lines or the capacitance values of the shunt capacitors can be adjusted in order to shift this frequency to 123.2 MHz. After tuning the Mode 1 frequency to the Larmor frequency, both of the ports of the coil need to be matched to the universally common 50 Ω impedance in order to transfer as much power to the coil as possible.

On the other hand, it should be recalled that the aim is not to construct an inductively coupled TEM coil. Rather, our objective is to build an 8-port TEM array, which requires the line elements to be decoupled (isolated). To this end, input port matching of the TEM coil is skipped, and we proceeded with decoupling process to construct our 8-port TEM array.

3.2.3 From Coil to Array: Decoupling the Line Elements

The term "decoupling", which can also be characterized as the extent to which the ports are isolated from each other is a very common issue in multi-port RF networks. In theory, the magnitude of the off-diagonal elements of the scattering matrix of an N-port network ($|S_{mn}|$, $m \neq n$)) needs to be equal to zero for its ports to be considered as "decoupled". In the context of symmetric and reciprocal passive microwave networks such as TEM coils, this is generally accompanied with the vanishing transfer impedances such that $Z_{mn} = 0$.

As the microstrip transmission lines in the designed coil are located parallel to each other, they perform a mutual inductance effect on each other. This effect acts as if there is an artificial inductor (hence an artificial impedance) is connected between the transmission lines. For an eight channel TEM array, the mutual inductance between non-adjacent elements are generally neglected and the inductive coupling is assumed to occur only among adjacent microstrip lines. Therefore, this mutual inductance between the transmission lines is eliminated by placing "decoupling capacitors" among the rear ends of the transmission lines, as depicted in figure (3.7) Capacitance values of these decoupling capacitors (C_d) are given as [2]:

$$C_d = \frac{1}{\omega^2 M} \tag{3.4}$$

where, ω is the Larmor frequency and M is the mutual inductance. Analytically calculating this mutual inductance is possible for co-planar microstrip lines, however, for the case of the designed TEM array, the mutual inductance calculation tends to become horrendous. Furthermore, the place at which adjacent microstrips are "artificially" connected by inductors is unclear and subject to model assumptions.

In practice, the capacitance values of the decoupling capacitors for head-sized TEM arrays for 3T are generally in the range 0.5 - 2.5 pF. Therefore, parameter sweep in Comsol Multiphysics was used in order to optimize the value of the capacitance. When the input ports of the TEM coil is not matched, a capacitance

value of 1 pF gives $S_{21} \approx S_{32} \approx ...S_{87} \approx -65dB$, which turned out to be the optimal capacitance value for the decoupling capacitors.

It should be noted that the port decoupling is an important and challenging issue for the coils having more than eight ports. More advanced circuitry like ladder networks, which also consider the coupling between non-adjacent line elements are introduced in commercially available TEM arrays. On the other hand, the used decoupling network turned out to be sufficient for our purpose.

3.2.4 From Coil to Array: Matching the Input Ports

Considering the coil as an eight port symmetric, reciprocal and passive network, it would be impossible to match it from all of its ports if no loss is introduced [38].

In the environment of RF engineering, on the other hand, the required loss will obviously not be coming from a resistor as it will distort the overall noise figure. In such a network without any resistive elements, the loss will be brought forth by the conductive object ($\sigma > 0$) to be imaged, located inside the coil. This method of matching is generally done when a conductive phantom is located inside the coil. Therefore, input matching is accomplished by putting a cylinder of radius 11 cm in the center of the coil. The cylinder has $\epsilon_r = 80$ and $\sigma = 0.5S/m$ in order to have similar electrical properties with human tissues.

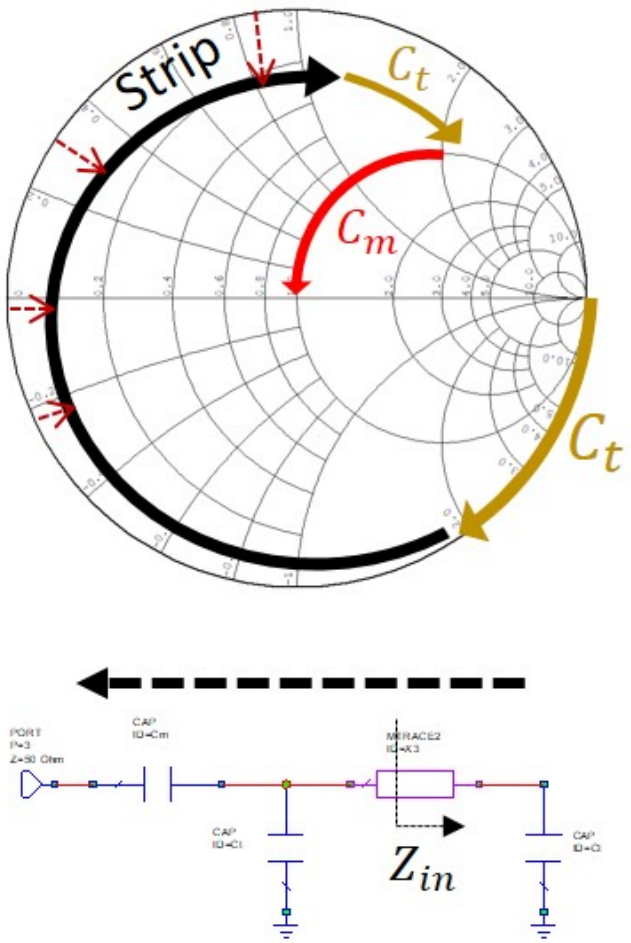

Figure 3.6: Input matching process of a single line element of the coil, explained on the Smith Chart. C_t represents the tuning and C_m denotes the matching capacitor. "Strip" refers to the transmission line. The direction of the arrows shows the movement of the input impedance from "open" to 50 Ω.

Input matching of all of the ports are accomplished by adding series matching capacitors (C_m) to the input ports of the coil, such has the ones in figures (3.6) and (3.7). The overall matching process of a single line element is illustrated with the use of Smith Chart in figure (3.6). Just as in figure (3.2), the tuning capacitors (C_t) and the transmission line ($Strip$) are rotating the input impedance towards the port. On the other hand, one very important observation is that in contrast to the lossless $\lambda/2$ resonator, the input impedance seen on the strip gets more and more towards the interior of the Smith Chart, as we move towards the port,

as emphasized by the dashed red arrows. The physical meaning of this movement is that the "Real" part of Z_{in} increases as we move towards the port as more loss is introduced to the microstrip line by the conductive phantom. After moving the impedance to the proper position with tuning capacitors and the strip, a proper matching capacitor is used to match the input impedance of the port to 50 Ω.

3.2.5 Finalized Coil and Simulation Results

To this end, the final structure of the coil in Comsol simulation environment is depicted in figure (3.7). The tuning and decoupling capacitors, (C_t and C_d) shown in figure (3.7), are constructed using the proper dielectric constants for the materials between two perfect electric conductor plates. On the other hand, the "lumped element" boundary condition of Comsol Multiphysics is used for the series matching capacitors, in order for geometrical suitability. The final dimensions and capacitance values of the coil are depicted in table (3.2).

ϵ_r	Z_0	w_s	h	w_g	l	C_t	C_d	C_m
3.6	50 Ω	2 cm	1 cm	12.56 cm	28 cm	31.5 pF	1 pF	2.5 pF

Table 3.2: Design parameters of the coil after tuning, matching and decoupling processes.

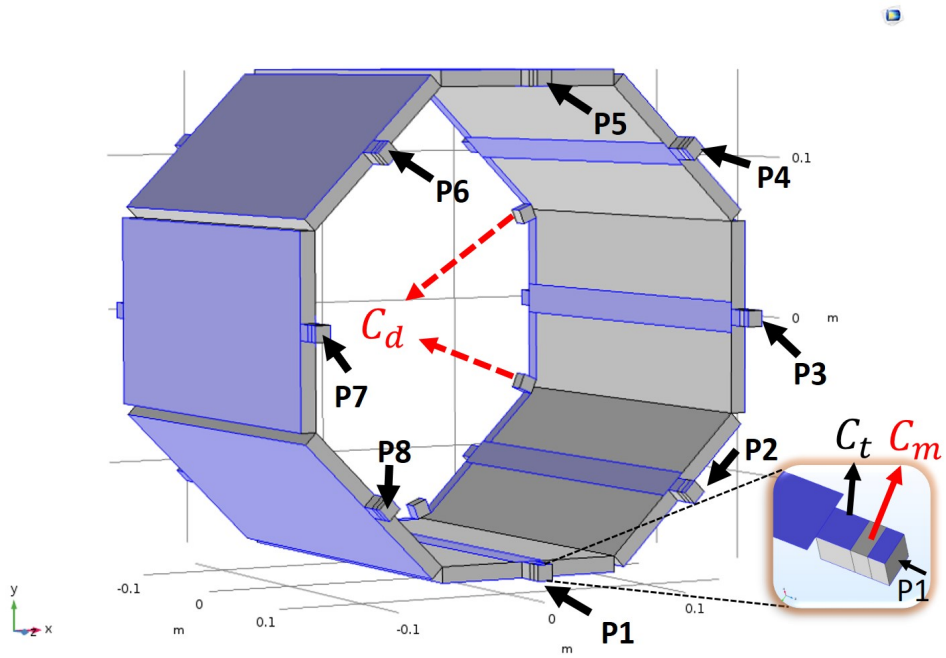

Figure 3.7: 8 channel TEM array, used in simulations. The purple boundaries indicate the metal layers and P1–P8 indicate the driving ports of the array. C_t and C_d are the tuning and decoupling capacitors, C_m is the series connected, lumped element defined, surface matching capacitor.

The input impedances of the eight ports of the TEM array are shown on the Smith Chart representation in figure (3.8), at 123.2 MHz. The complete S-matrix with respect to a reference impedance of 50 Ω is also shown on the same figure with color codes. As it can be seen, all of the the reflection coefficients of the ports ($S_{11}, S_{22}...S_{88}$) have values less than -30dB (technically around -40dB), indicating a very good input matching. On the other hand, the worst decoupling turns out to be between ports 1 and 3 having an approximate value of $-12dB$ which is sufficient.

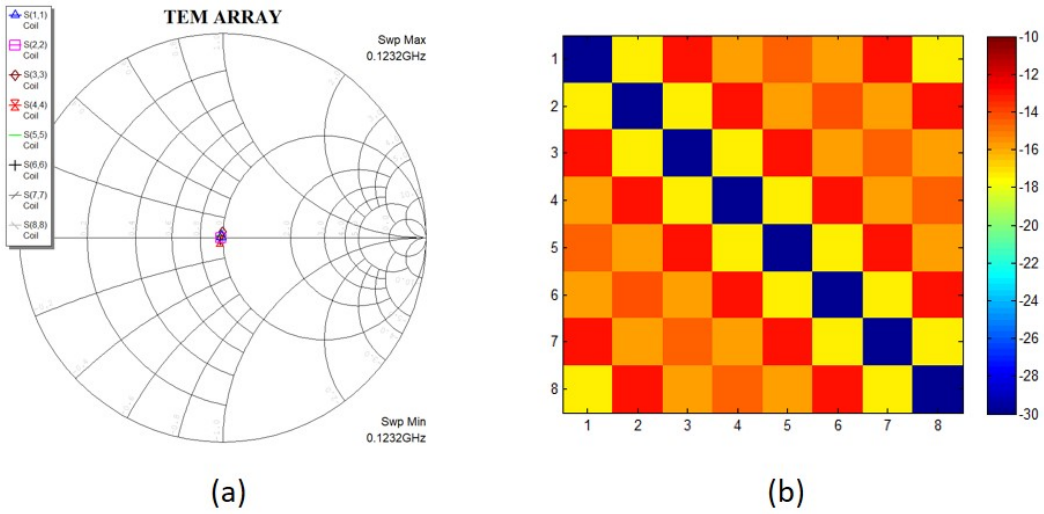

Figure 3.8: (a): The input impedances of the eight ports shown on smith chart. (b): The complete S-matrix (in dB units) of the TEM array at 123.2 MHz with a reference impedance of 50 Ω. Color scale is saturated at -30 dB in order for better visualization of the non-diagonal elements..

With the finalized coil construction in simulation environment, the B_1^+ field distributions for the one-channel only drive cases and multiple quadrature excitation configurations are depicted in figure (3.9). This figure demonstrates the B_1^+ fields just in the conductive phantom, used for matching, as described in the previous section. In this case the "multiple quadrature drive" corresponds to the excitation configuration in which each line element is driven with 45° phase increments and "one-channel only" drive refers to the n^{th} ($n \in \{1, ..., 8\}$) channel being individually driven with zero phase offset when all the other ports are terminated with their reference impedance (50 Ω).

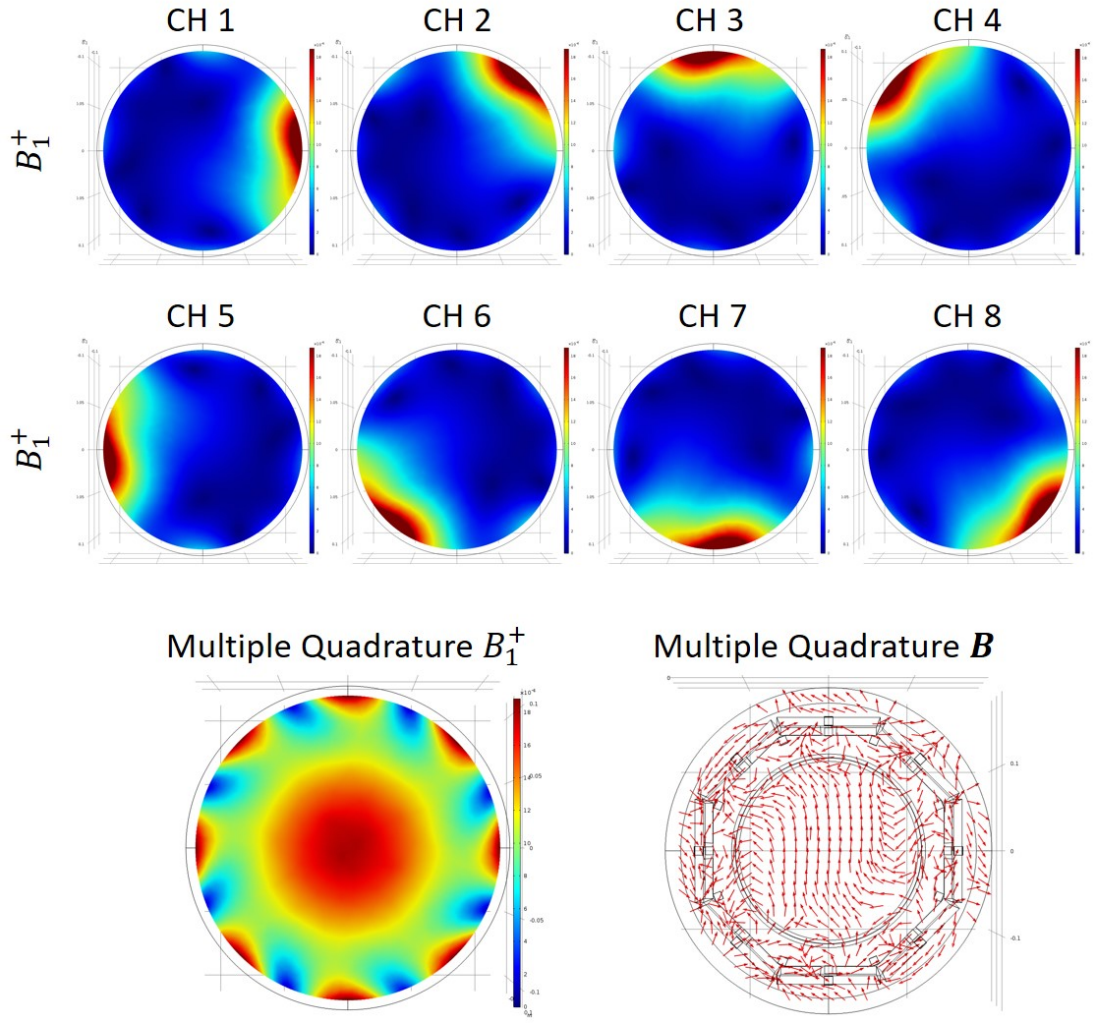

Figure 3.9: B_1^+ distributions for the one-channel only drive cases are given on the top, when each of channel is individually driven. Bottom two figures demonstrate the B_1^+ and $\boldsymbol{B}$ field distributions for the multiple quadrature excitation.

As it can be seen in figure (3.9), the one-port only drive cases generate a high B_1^+ magnitude in their neighbouring regions and the field magnitude turns out to be low at the regions far away from the driven port. This is a corollary of the decoupling process as it prevents current induction in the other ports when a single port is excited. In the multiple-quadrature excitation configuration, the generated B_1^+ magnitude at the interior region of the phantom demonstrates the well-known "central brightening" pattern, in which the B_1^+ magnitude reaches a peak value at the center of the symmetrical phantom. The $\boldsymbol{B}$ field distribution,

as it can be seen, is again, directed towards the upper side of the coil, however, the field lines tend to curve while they are entering the cylindrical conductive phantom. This is a result of the behavior of magnetic fields at region boundaries.

Chapter 4

Fabrication of the TEM Array

Design and simulation-based implementation of the microstrip element based eight-channel TEM array was described in the previous chapters. As mentioned, the ultimate objective on designing such a decoupled array is to perform a B_1^+ shimming (adjustment) inside the object to be imaged. On the other hand, the initial steps in the implementation of this TEM array is to acquire MRI images with it. Therefore, the quadrature drive is used in the experiments, being described in this chapter. Starting with the construction of the TEM array, this chapter also explains the required RF front-end to use it in an MRI scanner. Furthermore, the confronted practical issues have also been explicitly addressed.

4.1 Construction and Measurements of the TEM Array

Dielectric material of the coil, which gives it the octagon shape is chosen to be plexiglass, having an approximate relative dielectric constant as $\epsilon_r = 3.6$. The microstrip transmission lines on the coil are 2 cm in width and the dielectric thickness is chosen to be 1 cm in order for achieving a characteristic impedance of approximately 50 Ω. Capacitance values of the shunted tuning capacitors at

both ends were designed to be 31 pF in simulations, however 27 pF capacitors are used at both ends of the coil. In parallel to the 27 pF capacitors on the back end of the coil, variable capacitors (Knowles Voltronics 1-23 pF Non-Magnetic 750 V Trimmer, Part Number:NMAJ25HV) are used for tuning. Furthermore, the same type of variable capacitors are used in series for matching in the front end of the array. Using very sensitive and precise matching and tuning capacitors allowed us to perfectly match the ports to 50 Ω without sacrificing from the decoupling. After construction, we had a special casing for the TEM array, designed by "Artı Boyut" company, located in Cyberpark area of Bilkent University. This casing, being constructed in a 3-D printer with the material "PLA" is required in order for structural rigidity and electronic safety of the coil. The bare coil, its capacitors and the coated coil are depicted in figure (4.1).

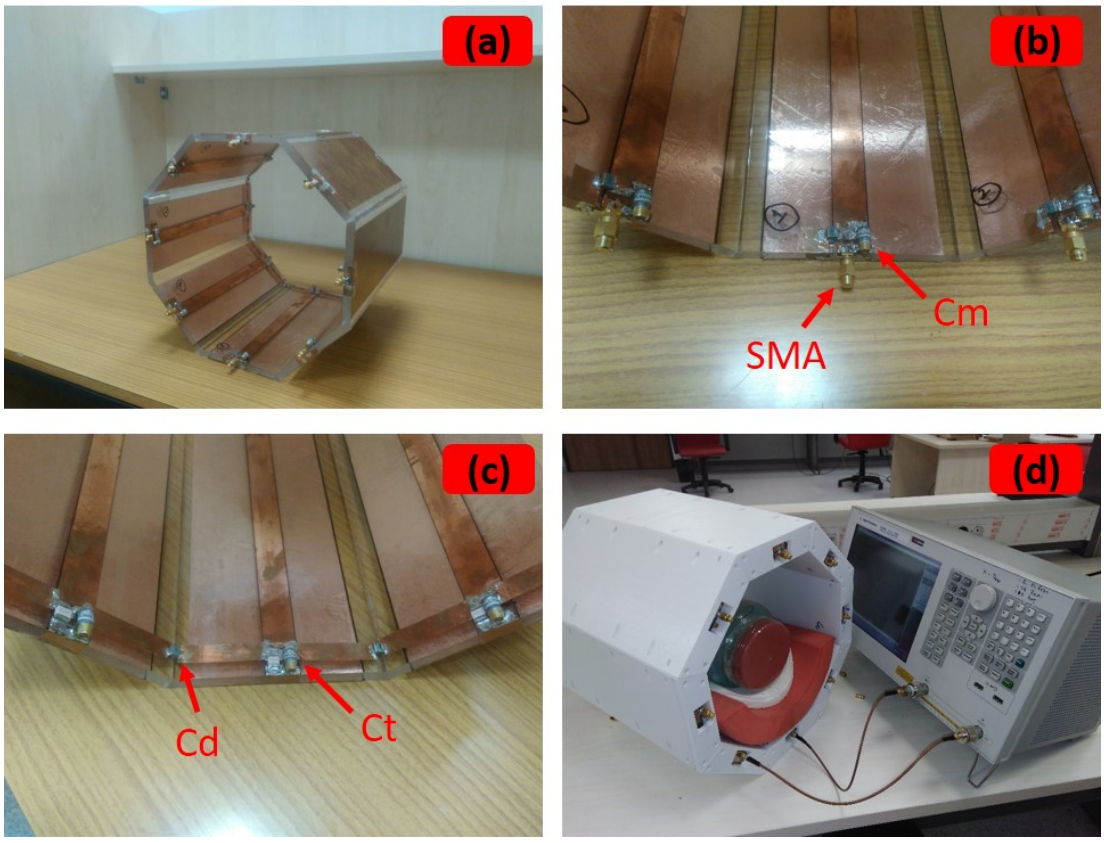

Figure 4.1: The TEM array with and without casing: (a): Constructed 8 channel TEM array. (b),(c): The bare structure viewed from front and back end respectively. C_t and C_d are the tuning and decoupling capacitors, C_m is the matching capacitor. (d): The coated coil being shown in measurements.

S-parameters of the loaded coil are measured with a vector network analyzer (Agilent ENA E5062A 300 kHz - 1.5 GHz). The diagonal and non-diagonal elements of the S-matrix, characterizing the input reflection coefficients and port decoupling respectively, are depicted in figure (4.2). As it can be seen, all of the reflection coefficients $(S_{11}, S_{22}, ..., S_{88})$ attain a value of approximately -40 dB at 123.23 MHz and the isolation of the ports are at -14 dB at the worst case, which is sufficient [5, 40, 41].

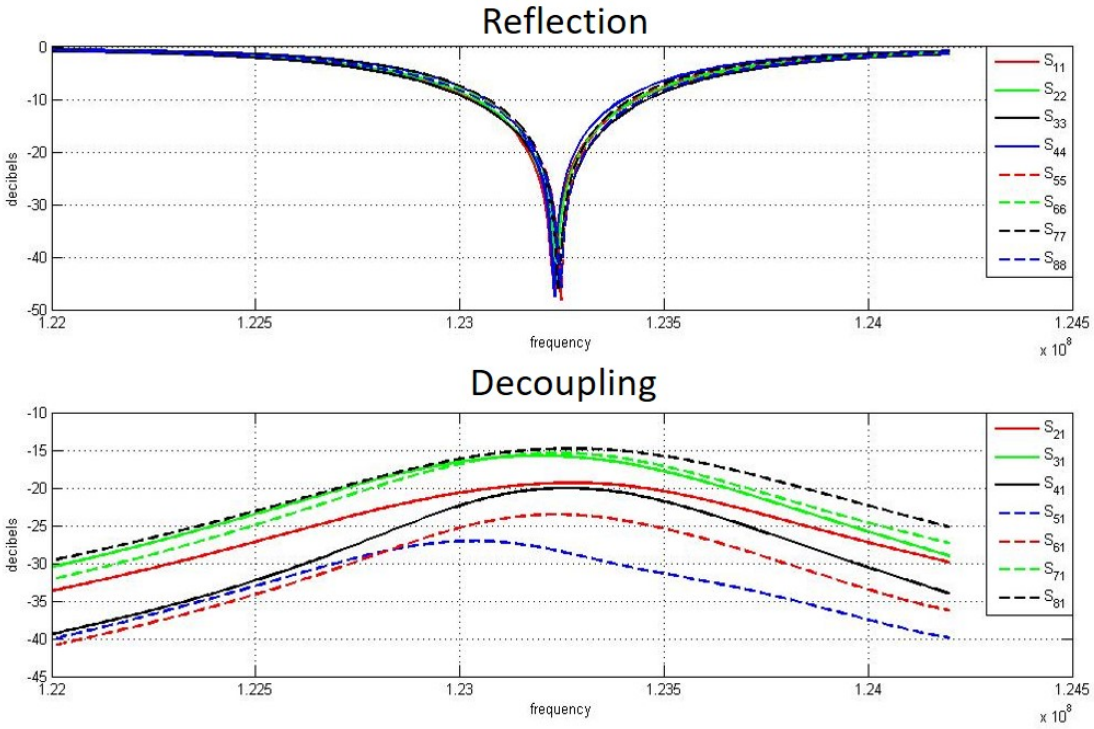

Figure 4.2: S-Parameters of the constructed coil. (top): $S_{11}, S_{22}...S_{88}$ Parameters, showing the reflection coefficients and (bottom):$S_{21}, S_{31}...S_{81}$, denoting the decoupling coefficients.

Furthermore, having a narrow bandwidth did not obstruct the experiments as the MRI scanner is capable of applying the RF signal with a highly accurate frequency (which is 123.23 MHz). To further illustrate the reflection coefficients and the input impedances at each port, $(S_{11}, S_{22}, ..., S_{88})$ are also shown on the Smith Chart in figure (4.3). As it can be seen, each frequency versus impedance curve on the Smith Chart are nearly identical and individually have the impedance

behavior of a conventionally matched $\lambda/2$ resonator [38].

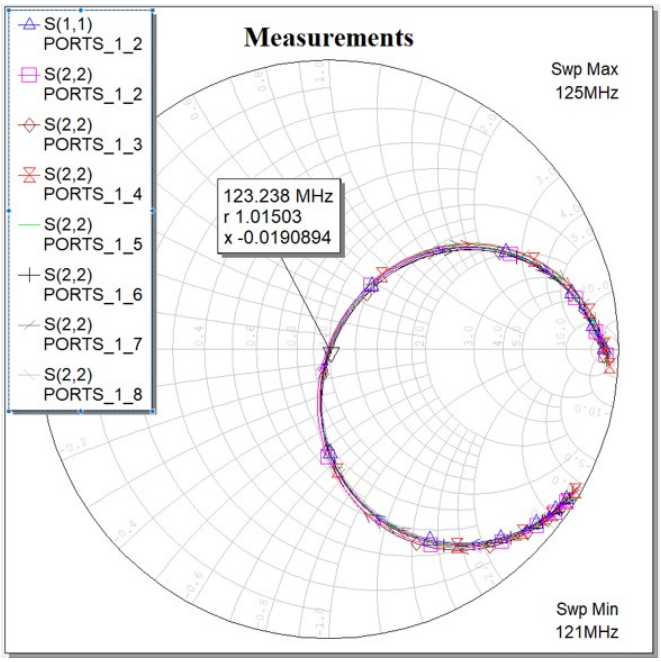

Figure 4.3: Reflection coefficients ($S_{11}, S_{22}...S_{88}$) on the Smith Chart.

4.2 RF Front End

The fabricated coil is successfully matched, decoupled and tuned, as explained in the previous section. On the other hand, an RF transmit-receive (T/R) switch is required to obtain MRI images as the array will be used both in transmit and receive operations (transceiver array). For this purpose, the T/R switch, being previously designed and fabricated by Taner Demir in UMRAM was used. The RF front end is conceptually very similar to the one in [41], however the one used in the current study is designed to resonate at 123.2 MHz. RF input phases during transmission are adjusted by using the eight channel transmit array system of Siemens Tim Trio 3T Scanner. The gains of the receive pre-amplifiers are in the range of 21-24 dB at an input source power of -25 dBm and the noise figures are in the range of 1.3 - 1.6 dB. Transmit/receive isolation of all of the eight channels of the RF switch are less than -25dB, which is acceptable. The

complete RF front end is shown in figure (4.4).

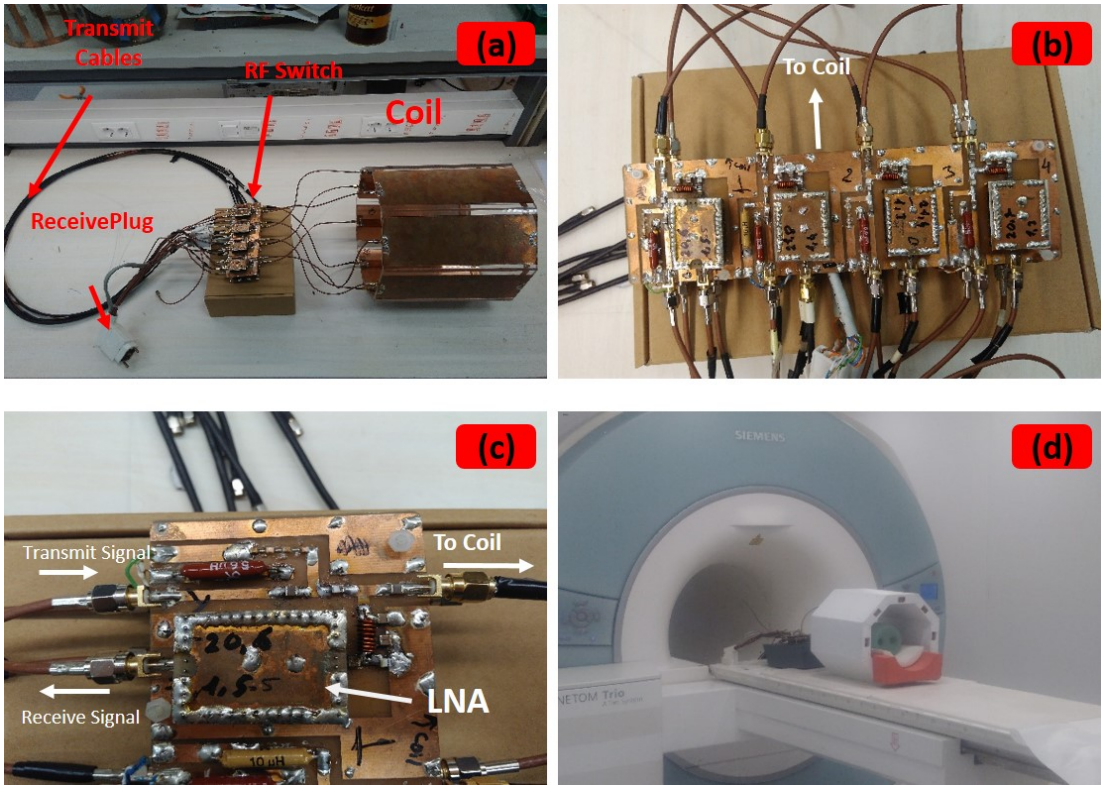

Figure 4.4: The complete RF front-end: (a): Front end with the bare coil. (b): T/R switch. (c): a single channel of the T/R swich. (d): The complete RF front end with the coil in MRI experiments.

4.3 MRI Experiments

In order to evaluate the imaging performance of the fabricated coil, MRI experiments have been conducted. As we are interested in the B_1^+ magnitude and phase, the steady state free precession (SSFP) and gradient recalled echo (GRE) images have been acquired with the coil. The sequence parameters are given in table (4.1).

Furthermore, it needs to be mentioned that the driving configuration in both SSFP and GRE sequences in this case is quadrature drive (45° current phase

increments between adjacent channels). Obtaining a quadrature drive, on the other hand, turns out to be more difficult than it seems, with the use of the hand made RF front end. Unfortunately, the transmit cable lengths and additional transmit phases of the RF front end (the RF switch and transmit cables) tend to differ from channel to channel. These phases were previously measured and reported by Taner Demir and Umut Gündoğdu in UMRAM. Including the phase offsets of the RF switch, its many different details are provided in appendix (A). These measurements of the RF front end turn out to be extremely significant as one wants to accomplish B_1 shimming or B_1 phase mapping inside the object to be imaged. These issues will be thoroughly addressed in the 6th chapter.

	FOV	**TE**	**TR**	**Slices**	**Voxel Size**	**Averages**	**Flip Angle**
SSFP	150 mm	2.34 ms	4.68 ms	2-D	1.2x1.2x5 mm	256 (32x8)	40 °
$\boldsymbol{GRE_1}$	150 mm	5 ms	1500 ms	2-D	1.2x1.2x5 mm	2	60 °
$\boldsymbol{GRE_2}$	150 mm	5 ms	1500 ms	2-D	1.2x1.2x5 mm	2	120 °

Table 4.1: MRI sequence parameters for SSFP and GRE sequences. Two different GRE sequences were used in order to get the B_1 map with the double angle method.

The agar phantom to be imaged inside the coil is made up of a background and two equivalent cylindrical anomalies. An agar- saline solution is used in the background, having 20 gr/l of agar, 2 gr/l of salt (pure $NaCl$) and 3 gr/l $CuSO_4$. On the other hand, the cylindrical anomalies include 6 gr/l of $NaCl$ and 3 gr/l $CuSO_4$. Our reason to use $CuSO_4$ at high concentrations is to reduce the decay constant (T_1) of the solution, which allows us to conduct the GRE executions with low TR values, such as 1500 ms. On the other hand, the saline concentrations having 2 gr/l of salt have an electrical conductivity of approximately 0.5 S/m while 6 gr/l of salt concentration yields a conductivity of 1 S/m [20].

The SSFP magnitude images are depicted in figure (4.5). As it can be seen, eight different SSFP magnitude images are acquired from each channel. With the use of quadrature drive and individual channel reception, the magnitude of SSFP images tend to increase towards the channel by which it is received.

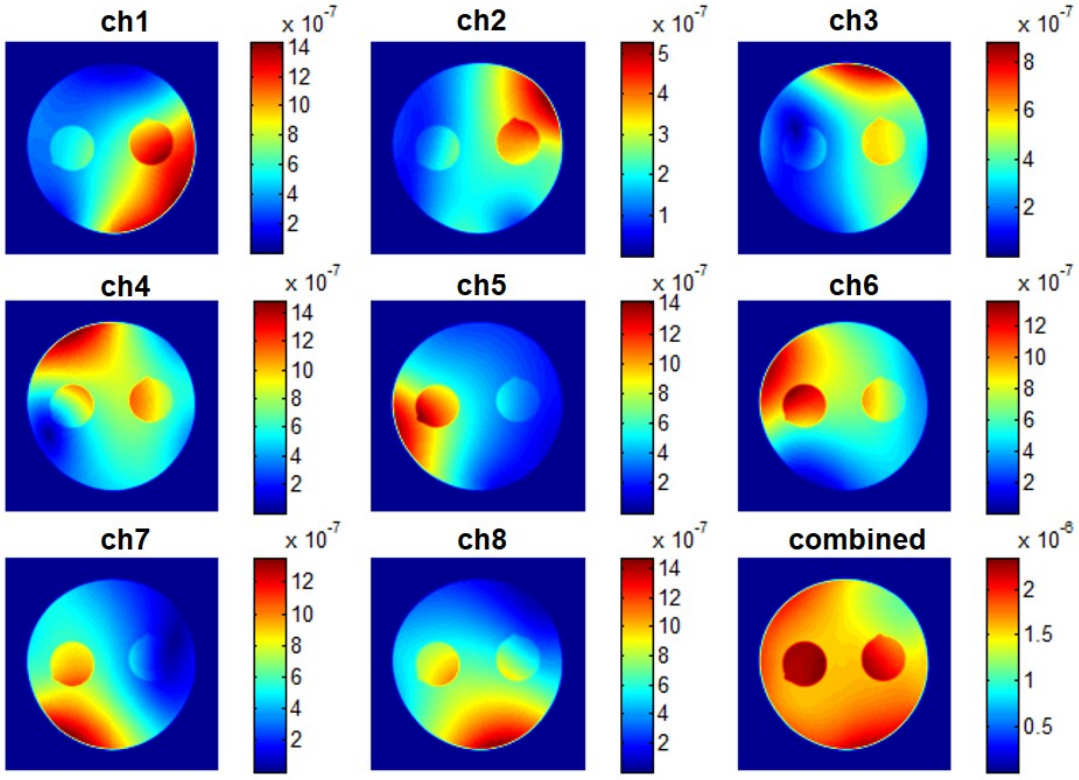

Figure 4.5: SSFP images of the phantom with anomalies. Quadrature drive is used during transmission and reception is accomplished from eight channels. "ch n" refers to the SSFP image obtained with the n'th channel. "combined" version demonstrates the merged magnitude image with the sum of squares method.

Commenting on the images acquired by each channel in figure (4.5), it should be noticed that color scales of each image is different. This is a result of the imperfections of the RF pre-amplifiers. As the pre-amplifiers connected to each channel have a different gain, the magnitude intensity of each image tends to be different from each other. Therefore, the combined magnitude image has a lower magnitude at the upper left corner, as it can be seen.

To consider the transmit performance of the coil, B_1 mapping was performed with the use of double-angle method. The technique requires us to acquire two successive GRE images with 60 ° and 120 ° flip angles, respectively. Both of

the channel-combined GRE images and B_1^+ map are depicted in figure (4.6). It should be noticed that the transmit field (B_1^+) magnitude demonstrates a central brightenning behavior, being slightly disturbed by the cylindrical conductive anomalies located inside the phantom.

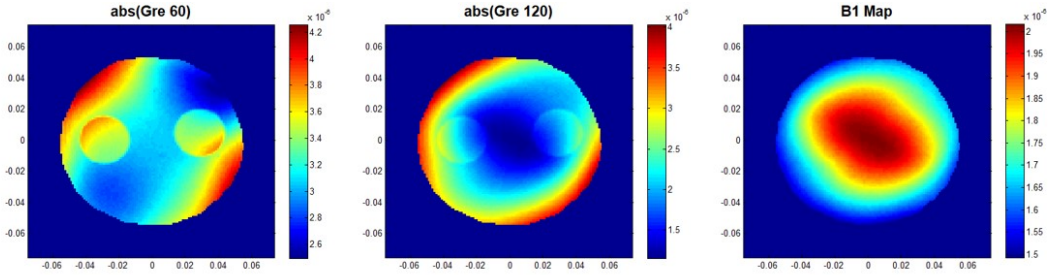

Figure 4.6: GRE images of the double angle method. "abs(60)" and "abs(120)" refer to the magnitude images of the experiments with 60° and 120° flip angles respectively. B_1^+ magnitude distribution is demonstrated in the leftmost image.

Acquisition of successful MRI images with the fabricated coil finalizes our coil implementation process. On the other hand, as mentioned in the introduction, our ultimate objective is to alleviate the LCF artifact from the conductivity images of MRI. Therefore, the subsequent chapters will focus on a simulation based artifact elimination method and its practical application will follow.

Chapter 5

Optimal RF Drive for Improved cr-MREPT

This chapter gives details about the artifact reduction algorithm that we designed for cr-MREPT studies. Commencing with the theory behind the cr-MREPT method, this chapter elucidates the reason of the LCF artifact and gives the logic behind the applied procedure. In continuation, simulation methods are explained and reconstruction results of three different simulation phantoms (including the head model) are given.

5.1 Theory

5.1.1 cr-MREPT Theory

The cr- MREPT method [20] is based on the solution of the following convection-reaction partial differential equation for the unknown "u" :

$$\boldsymbol{\beta} \cdot \nabla u + \nabla^2 H^+ u - iw\mu_0 H^+ = 0 \tag{5.1}$$

where $u = 1/\gamma, \gamma = \sigma + iw\epsilon$,

$$\boldsymbol{\beta} = \begin{bmatrix} \beta_x \\ \beta_y \\ \beta_z \end{bmatrix} = \begin{bmatrix} \frac{\partial H^+}{\partial x} - i\frac{\partial H^+}{\partial y} + \frac{1}{2}\frac{\partial H_z}{\partial z} \\ i\frac{\partial H^+}{\partial x} + \frac{\partial H^+}{\partial y} + \frac{i}{2}\frac{\partial H_z}{\partial z} \\ \frac{\partial H^+}{\partial z} - \frac{1}{2}\frac{\partial H_z}{\partial x} - \frac{i}{2}\frac{\partial H_z}{\partial y} \end{bmatrix}, \quad \nabla u = \begin{bmatrix} \partial u/\partial x \\ \partial u/\partial y \\ \partial u/\partial z \end{bmatrix}$$

This equation, having the convection term as $\boldsymbol{\beta} \cdot \nabla u$ and the reaction term as $\nabla^2 H^+ u - iw\mu_0 H^+$ can either be solved in three dimensions or it can be solved in two dimensions for only the slice of interest, by neglecting the derivatives of H_z, and the z-derivatives of H^+ as in [20]. When considered in two dimensions, equation (5.1) reduces to equation (5.2), which is given by:

$$\boldsymbol{F} \cdot \nabla u + \nabla^2 H^+ u - iw\mu_0 H^+ = 0 \tag{5.2}$$

where

$$\boldsymbol{F} = \begin{bmatrix} F_x \\ F_y \end{bmatrix} = \begin{bmatrix} \frac{\partial H^+}{\partial x} - i\frac{\partial H^+}{\partial y} \\ i\frac{\partial H^+}{\partial x} + \frac{\partial H^+}{\partial y} \end{bmatrix}, \quad \nabla u = \begin{bmatrix} \frac{\partial u}{\partial x} \\ \frac{\partial u}{\partial y} \end{bmatrix}$$

For this case, $\boldsymbol{F} \cdot \nabla u$ is the convection term and $\boldsymbol{F}$ is the "convective field". H^+ and therefore $\boldsymbol{F}$ are obtained from the simulations. It should be noted that the y-component of the vector $\boldsymbol{F}$ is the complex number i times its x-component. Therefore, in order to observe and analyze the properties of $\boldsymbol{F}$, it suffices to investigate F_x.

As explained in [20], equation (5.2) is discretized on a triangular mesh and a system of linear cr-MREPT equations is obtained with the number of equations being equal to the number of triangular elements in the mesh. In this case, the number of unknown "u"s is equal to the number of the nodes. The "u" values at the external boundary nodes are assumed to be known. It is observed that inaccurate boundary values distort the solution for only a few layers of nodes

towards the interior of the object. Conductivity and relative permittivity are extracted from the solution using $\sigma = Re\{1/u\}$ and $\epsilon_r = (1/w\epsilon_0)(Im\{1/u\})$.

It was reported in [20, 28] that the permittivity reconstructions of cr-MREPT tend to give overestimated results at the regions with higher conductivities compared to their surroundings and that permittivity reconstructions are much more vulnerable to noise contamination. Therefore, in contrast to the conductivity results, all of the relative permittivity reconstructions except for the ones in "homogeneous phantom" are obtained after filtering the B_1^+ data with a 2-D Gaussian filter having a kernel size of 3x3 and a standard deviation of 2.

When two sets of data are collected for the same object such as in padding studies [20, 29] or as in this study where data for normal drive and modified drive are collected, the two systems of cr-MREPT equations obtained using the two sets of data are simultaneously solved. The results obtained from this simultaneous solution are called "combined conductivity" and "combined permittivity" images.

5.1.2 Observations Regarding the LCF

As mentioned above, the LCF artifact, occurring at the regions where magnitude of the convective field $\boldsymbol{F}$ attains a value of zero (or a value comparable to noise), has a behavior characterized by abrupt and significant point-wise jumps at the EP reconstructions obtained by the cr-MREPT method.

To propose a solution based on shifting the LCF artifact, we make several observations on the relation between electric field, H^+ field, and the LCF region.

Considering the definition of F_x in equation (5.2) and using $(H^+ = (H_x + i.H_y)/2)$, one gets

$$F_x = \frac{1}{2}\Big[\frac{\partial H_x}{\partial x} + \frac{\partial H_y}{\partial y} + i(\frac{\partial H_y}{\partial x} - \frac{\partial H_x}{\partial y})\Big] \tag{5.3}$$

Using the fact that $\nabla \cdot \boldsymbol{H} = 0$ and assuming $\frac{\partial H_z}{\partial z}$ is negligible, we obtain the simplified expression

$$F_x \approx (i/2)(\partial H_y/\partial x - \partial H_x/\partial y) \tag{5.4}$$

Finally, using the z-component of the Ampere's law, one can show that

$$2iF_x = \gamma E_z \tag{5.5}$$

This equation implies that magnitude of the convective field $\boldsymbol{F}$ attains low values where γE_z, being the sum of conduction and displacement currents, is low. As the electric field, and hence the current density at a certain region drops it will no longer provide a B_1^+ contribution which would contain information for reconstructing the EP's at that region. This corollary guides us with the inference that we need to shift the region where the z-component of the electric field becomes low in order to shift the location of the LCF artifact.

Considering the conventional birdcage coil systems used in MRI RF transmission, the coil produces a B_1^+ or, equivalently a $\mu_0 H^+$ field with a maximum magnitude and minimum phase at the center, when a cylindrical and homogeneous electrical properties phantom is located inside. Furthermore, the magnitude and phase of the H^+ become more and more constant as we reach the center of the phantom. Regarding equation (5.4), therefore, it becomes not surprising to have an LCF artifact at the center of a homogeneous phantom due to the vanishing derivative terms. In this regard, our proposal for shifting the LCF region is to perform a B_1^+ modification with the goal of having a varying $B_1^+ = \mu_0 H^+$ magnitude at the middle region of the object. The magnitude-based B_1^+ modification will be explained in the following section.

5.2 Methods

5.2.1 B_1^+ Modification for Shifting the LCF Region

The B_1^+ modification inside the phantom was carried out with the magnitude and phase adjustment of the RF inputs at the channel input ports of the TEM array which is described in the next section. The procedure, which has been invoked in different studies such as [42, 43] is explained as follows:

We start by calling the B_1^+ distribution inside a region of interest, which is interior to our simulation phantom, as $\boldsymbol{B1}^+(V_1, \phi_1, V_2, \phi_2, ...V_8, \phi_8) = \boldsymbol{B1}^+(\boldsymbol{\theta})$, where V_n and ϕ_n such that $n \in \{1, 2, 3, 4, 5, 6, 7, 8\}$ are the amplitudes and phases of the RF inputs, applied from the n'th port respectively. $\boldsymbol{B1}^+$ is the discretized complex B_1^+ distribution vector (organized as one column) and $\boldsymbol{\theta}$ is the RF input parameter vector such that $\boldsymbol{\theta} = [V_1, \phi_1, V_2, \phi_2, ..., V_8, \phi_8]^T$. Due to the superposition principle, we can say that the B_1^+ field, generated by the eight RF input channels simultaneously, is equal to the sum of the B_1^+ fields generated by the individual RF input channels as in equation (5.6).

$$\boldsymbol{B1}^+(\boldsymbol{\theta}) = \sum_{n=1}^{N_{channel}} V_n e^{(i\phi_n)} \boldsymbol{B1}^{\boldsymbol{n}+}(1V, 0^\circ) \tag{5.6}$$

where, $N_{channel}$ is the number of RF channels (ports) and $\boldsymbol{B1}^{\boldsymbol{n}+}(1V, 0^\circ)$ is the B_1^+ distribution due to the n'th individual channel, when all the channels except for the n'th channel are reference impedance (50 Ω) terminated (not driven by RF signal) and the n'th channel is driven with RF amplitude and phase values of $1V$ and 0°, respectively. In this regard, we can define the $\boldsymbol{\theta}$ dependent cost function as:

$$C(\boldsymbol{\theta}) = \sum_{i=1}^{M} (|B1_i^+(\boldsymbol{\theta})| - |B1_i^{+,goal}|)^2 \tag{5.7}$$

where, M is the total number of elements in the $\boldsymbol{B1}^+(\boldsymbol{\theta})$ vector, $B1_i^+(\boldsymbol{\theta})$ is the i'th element of the $\boldsymbol{B1}^+(\boldsymbol{\theta})$ vector and $B1_i^{goal}$ is the i'th element of the $\boldsymbol{B1}^{+,\boldsymbol{goal}}$ vector which represents the desired (objective) B_1^+ distribution.

Objective of the parameter adjustment process is to minimize the cost function with regard to the RF-input vector $\boldsymbol{\theta}$. For this purpose, the Newton Minimization procedure, in particular, the steepest descent method was applied by using the "optimization toolbox graphical interface" of MATLAB (Mathworks, Natick, MA, USA). The cost function, defined in equation (5.7) allows us to manipulate the magnitude of the transmit field, not taking into account its phase.

On the other hand, one very important point of this optimization procedure is the selection of the $\boldsymbol{B1^{+,goal}}$ vector. This selection is the main aspect that shifts the LCF artifact and it will be further discussed in the following sections.

5.2.2 Simulation Phantoms

In order to apply the algorithm, two different cylindrical simulation phantoms and a head model, as shown in figures (5.1) and (5.2) were used. The first phantom, or the so-called "homogeneous phantom" is an object in which $\sigma = 0.5 S/m$ and $\epsilon_r = 80$ everywhere (for region I, shown in figure (5.1)). For the second phantom, the phantom with anomalies, there are three regions II, III and IV in which $\sigma = 0.5$ S/m, 0.85 S/m, 1.25 S/m, and $\epsilon_r = 80$, 50, 50 respectively. Radii of both cylindrical phantoms are chosen to be 11 cm, however, data is taken from an internal 7-cm radius region. Heights of these phantoms are 30 cm and the central horizontal slice is the z=0 slice. For both of the phantoms, relative permeability is taken as $\mu_r = 1$.

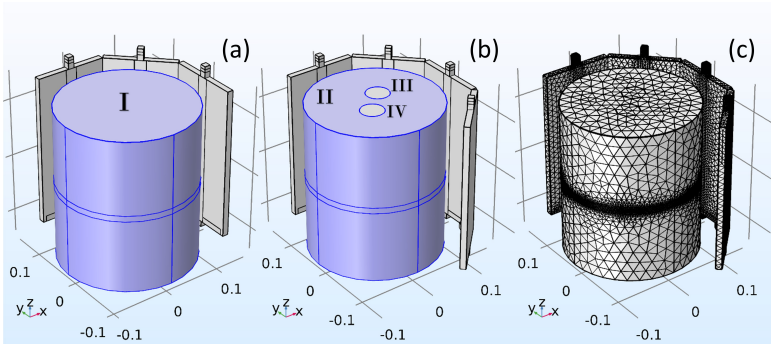

Figure 5.1: The simulation phantoms, shown inside the TEM array. (a) depicts the homogeneous phantom in which EPs are constant everywhere and (b) shows the phantom with two cylindrical anomalies. Regions I and II have $\sigma = 0.5$ S/m and $\epsilon_r = 80$. Regions (III) and (IV) have conductivities of $\sigma = 0.85$ S/m and $\sigma = 1.25$ S/m respectively, and relative permittivities of $\epsilon_r = 50$ for both. (c) demonstrates the mesh distribution for both phantoms. Only three line elements of the coil are shown for better visibility of the phantom.

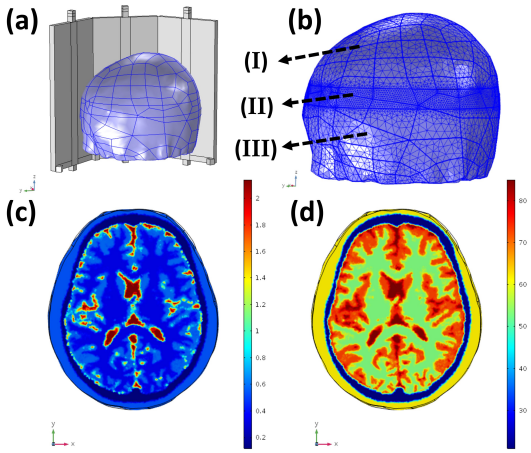

Figure 5.2: The localization and mesh distribution of the brain phantom in (a) and (b) respectively. The coarser mesh regions are I and III whereas the finer mesh region is shown by II. Conductivity (σ) and relative permittivity (ϵ_r) distributions at the central slice (z = 0, middle slice of region II) of the brain phantom are shown in (c) and (d) respectively.

The reconstruction algorithm was tested for the z = 0 slice. Constructing the mesh of the phantom and coil, tetrahedron based, variable size mesh has been used. The maximum element size was set to be 1.75 mm for the regions inside

the phantom where $-0.5cm < z < 0.5cm$ and inside all of the capacitors, and 1 cm for the remaining parts of the phantom and for the dielectric regions of the coil.

Analyzing the performance of the proposed algorithm on a more sophisticated and more realistic simulation phantom, a 3-D head model (brain phantom) simulation was found to be necessary [21, 44]. Localization and mesh distribution of the 3-D head model inside the TEM array is depicted in figure (5.2). Just like the other cylindrical phantoms, there is a central region (region II) of thickness 1 cm, having the finest mesh distribution in order to get the data with minimal noise. The maximum tetrahedral element size at the coarser regions (I and III) are chosen to be 1 cm whereas it is 1.75 mm at the finer region (II). The mesh size on the coil and at the surrounding air regions are the same as the ones in the previously described simulations.

The head model shown in figure (5.2) has internal conductivity and permittivity distributions, being compatible with the conductivity and permittivity of the internal regions of a human head. Being segmented into five tissues, namely cerebrospinal fluid (CSF), white matter (WM), gray matter (GM), skull and scalp, the approximate conductivity distributions of these tissues are respectively given as 2.14, 0.34, 0.59, 0.12 and 0.54 S/M and their approximate relative permittivity values are given as 84, 52, 73, 21 and 62 [11, 44, 45]. The conductivity and relative permittivity distributions, shown at the center slice (z=0) of the brain phantom are also demonstrated in figure (5.2).

5.3 Results

5.3.1 EP Reconstructions Obtained with the Normal Drive

For the homogeneous cylindrical phantom, B_1^+ magnitude, F_x magnitude and EP reconstructions using the cr-MREPT method are shown in figure (5.3) for the case where the coil is driven by 1 Volt of peak amplitude and 45 degree phase increment between the adjacent ports of the TEM array. This driving case will be referred to as the "normal drive" (quadrature drive) in the subsequent sections.

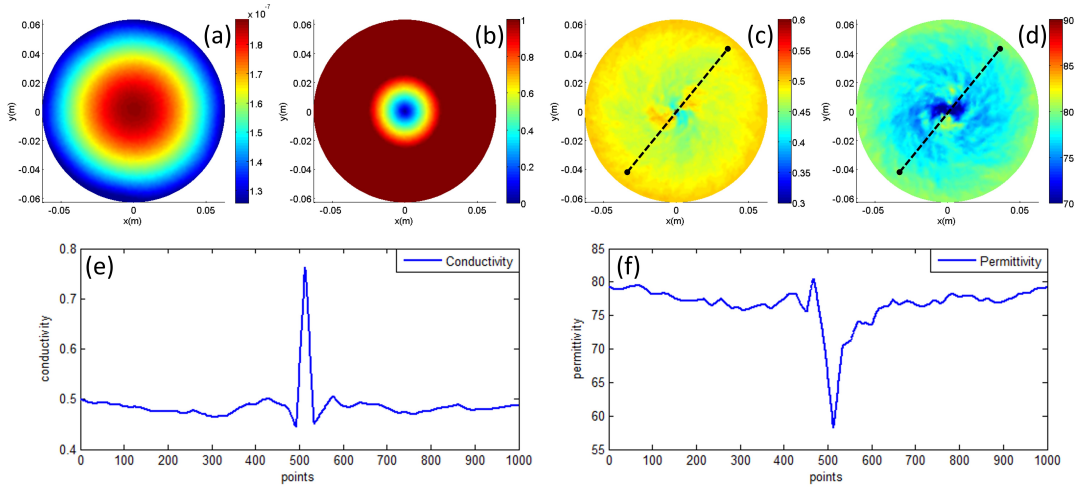

Figure 5.3: The B_1^+ magnitude, F_x magnitude, conductivity reconstruction (S/m) and relative permittivity reconstruction given in (a),(b),(c),(d) respectively. (e),(f) shows profile plots of conductivity and relative permittivity along the dashed lines on (c) and (d).

As it is clear from figure (5.3), the place at which the convective field magnitude significantly decreases is the center region and at that region, the abrupt positive and negative jumps at the EP reconstructions refer to the classically known "LCF-artifact". Furthermore, slow variations in the EPs around the LCF artifacts, extending over larger regions, are observed in figure (5.3c) and (5.3d). This phenomenon is called the "global bias" on the EP reconstructions, being

obtained by the cr-MREPT method [16].

5.3.2 The Modified B_1^+ Distribution

In order to shift the location of the LCF regions, a proper $B_1^{+,goal}$ ($\boldsymbol{B1^{+,goal}}$ is the discretized single-column version of the continuous $B_1^{+,goal}$) needs to be specified. Deciding on that, results of using different $B_1^{+,goal}$ distributions as well as the results of different shimming methods (described below) have been considered and compared.

Among the cases covered in this study, the $B_1^{+,goal}$ magnitude in the ROI shown in figure (5.4), which has high B_1^+ magnitude on one half and a low B_1^+ magnitude on the other half is chosen as the best distribution. The value of the B_1^+ magnitude in the higher half of the goal distribution (high field region), is chosen to be equal to the maximum B_1^+ magnitude value of the homogeneous phantom when the normal drive is used. For the lower part, (low field region) B_1^+ magnitude is assigned as one-tenth of the value in the higher part. By choosing such a $B_1^{+,goal}$ distribution, it is obviously not expected to obtain a modified B_1^+ distribution with a discontinuous transition in the middle due to the fact that electromagnetic wavelength in the phantom with $\epsilon_r = 80$ is approximately 27 cm (at 123.2 MHz). The purpose is to force the modified B_1^+ distribution to have a relatively sharp variation in the middle region.

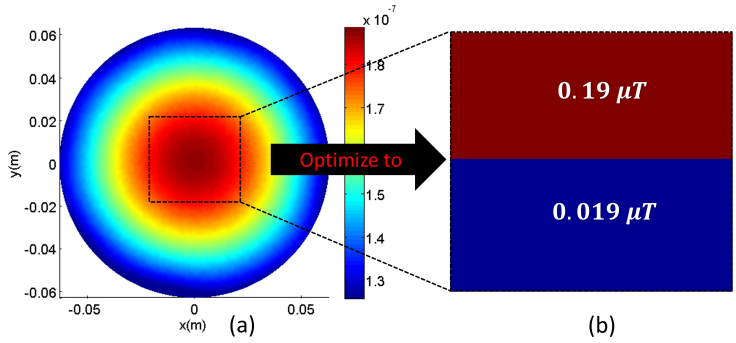

Figure 5.4: (a): a general B_1^+ magnitude image of a circular phantom of constant conductivity and permittivity. The central region in (a) (the indicated square) is the region where $B_1^{+,goal}$ is specified. (b): The optimization goal for the B_1^+ magnitude.

As different $\boldsymbol{B1^{+,goal}}$ distributions and different shimming methods are considered, their practical feasibility turns out to be crucial.

One physical limitation in this regard is that the ratio between the high field and low field regions need to be as low as possible in order to avoid significant signal to noise ratio (SNR) differences between them for the viability of implementation in an MRI scanner. Throughout our trials, as shown in figure (5.5), it has been observed that a ratio of two (2x) is not sufficient to significantly shift the LCF regions. On the other hand, a ratio of five (5x) yields a nicely shifted LCF region for the homogeneous phantom, though it does not substantially shift these regions for more complicated phantoms, such as the brain model. Consequently, a ratio of ten (10x) has been found as the most stable and efficient one in terms of sufficiently shifting the LCF regions away from the center and allowing accurate EP reconstructions at the center of each and every phantom. The resultant $|B_1^+|$ and $|F_x|$ distributions for the aforementioned cases are juxtaposed in figure (5.5).

Another physical obstruction is that the transmitter array of an MRI scanner may not be able to send the desired voltages to the input ports of the RF coil (due to imperfections on input matching) hence the peak amplitude ratios among different inputs should not be arbitrarily large. In order to avoid this issue, a

phase-only parameter adjustment method for attaining the $B_1^{+,goal}$ with a ratio of ten between the high and low field regions has been used. In this case, the same optimization algorithm was conducted where the amplitudes of the RF inputs were forced to be the same. However, this procedure also turned out to be insufficient for significantly shifting the LCF regions, as shown in figure (5.5).

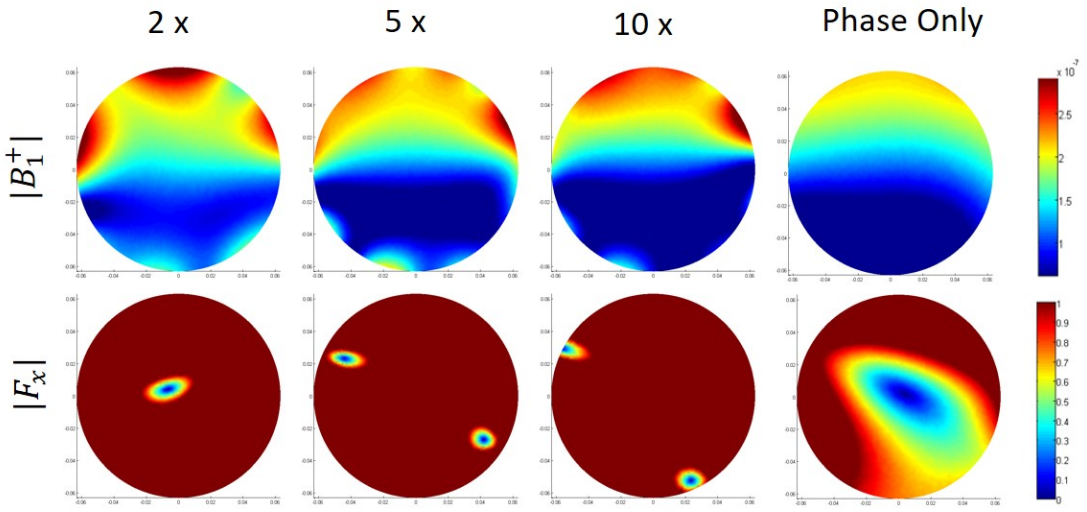

Figure 5.5: The B_1^+ magnitude (Tesla) and F_x magnitude distributions for the 2x, 5x, 10x cases as well as for the phase-only optimization methods.

To this end, the magnitude and phase values of the port RF inputs for 10x case are depicted in table (5.1). This driving configuration is explicitly referred to as the "modified drive" (non-quadrature drive) configuration.

Ports	**1**	**2**	**3**	**4**	**5**	**6**	**7**	**8**
Magnitude (V)	9.5	11.8	9.4	8.7	7.6	10.7	12.1	7.8
Phase (Rad)	-2.6	-2.7	-2.9	-2.5	-2.5	-2.5	-3.0	-2.8

Table 5.1: RF input signal magnitude and phase values for the modified drive. These values are the exact ones acquired with the modification algorithm. However, mean value of the phases is irrelevant and can be subtracted while using them.

5.3.3 The Combined EP Reconstructions

Having acquired the B_1^+ distributions from the normal and the modified drive configurations, our objective is to make simultaneous use of the two datasets to obtain the so-called "combined reconstructions".

The combined EP reconstructions, as well as the EP reconstructions from the modified drive only are shown in figure (5.6) for the homogeneous phantom. As it can be seen from figure (5.6a) and (5.6c), the modified drive spatially shifts the LCF artifact (as shown by the arrows in the figure) and the global bias on the EP reconstructions just as it shifts the LCF region as shown in figure (5.5), 10x case. When the combined reconstructions in figure (5.6b) and (5.6d) are considered, it is observed that the LCF artifacts are eliminated throughout the whole slice.

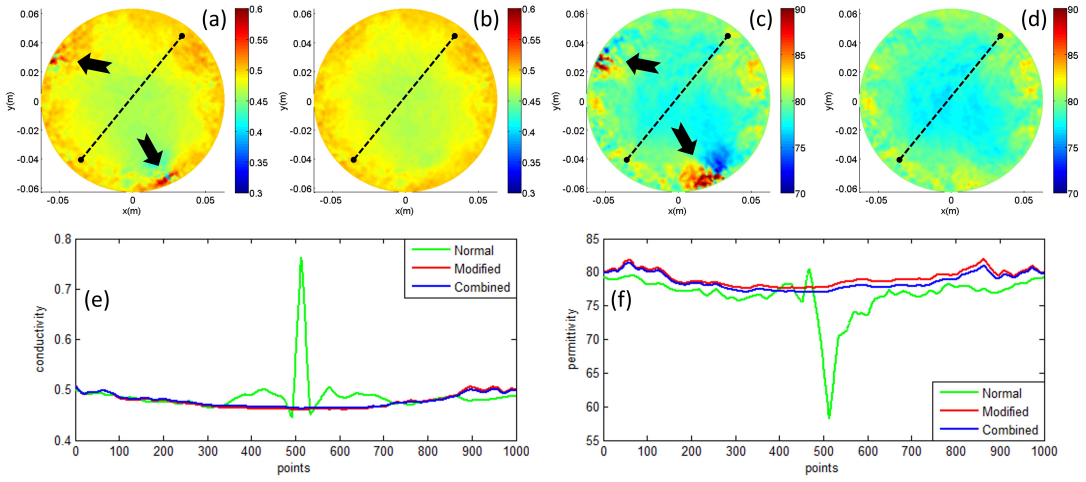

Figure 5.6: (a), (b): Modified and Combined conductivity reconstructions (in S/m), (c), (d): Modified and combined relative permittivity reconstructions. (e), (f): Profile plot of conductivity and relative permittivity reconstructions along the dashed lines on (a),(b),(c),(d) for normal drive, modified drive and combined cases.

As stated in the theory section, figure (5.7) shows the magnitude of the z component of the electric field for the normal and modified drive cases. Compared with the F_x distributions for normal and modified drive cases, this figure clearly demonstrates that there is a direct correlation between F_x and E_z as stated in

the theory section.

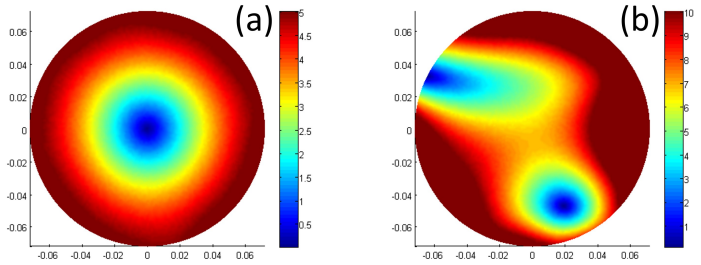

Figure 5.7: (a): E_z magnitude for normal drive, (b) E_z magnitude for modified drive. Both of the images belong to the homogeneous phantom.

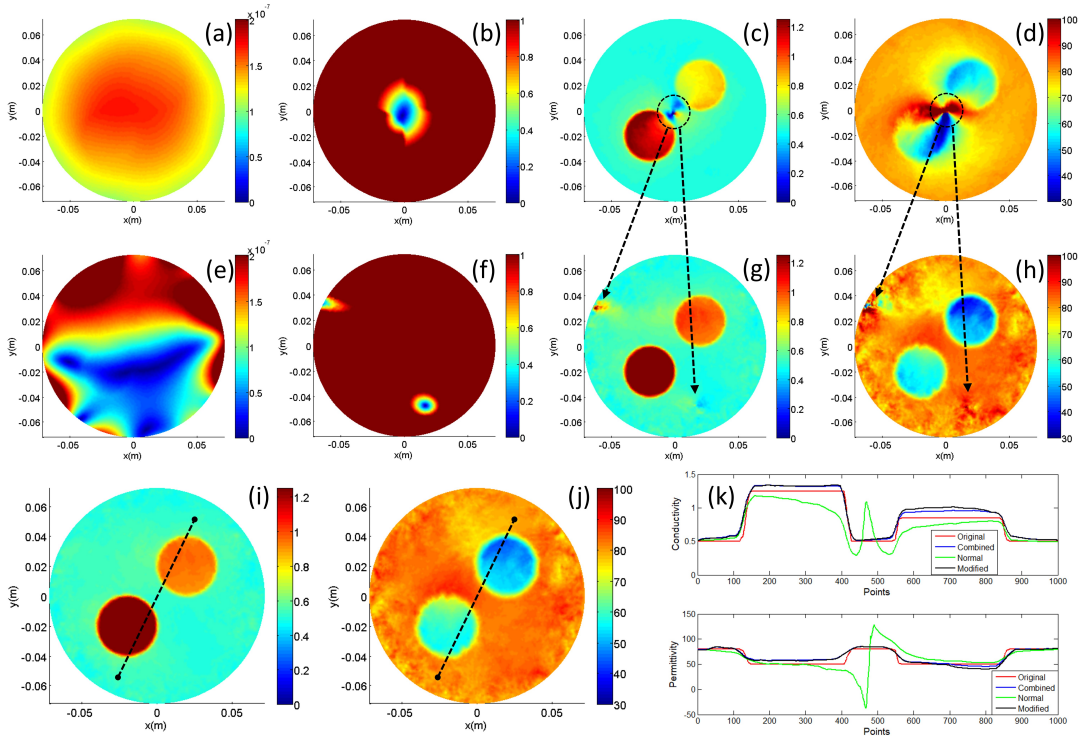

Figure 5.8: Results of the phantom with anomalies: (a,e): B_1^+ magnitude, (b,f): F_x magnitude, (c,g): conductivity reconstructions (S/m), (d,h): relative permittivity reconstructions for the normal and modified drive respectively, (i): combined conductivity reconstruction, (j): combined relative permittivity reconstruction and (k): Profile plots of original conductivity and relative permittivities (red) as well as profile plots of the reconstruction results for the normal drive (green), modified drive (black) and combined reconstruction (blue) cases. The profiles are taken along the dashed lines in (i) and (j).

After using the procedure of B_1^+ optimization for the homogeneous phantom, the exact same RF amplitude and phase values for the normal and modified drive cases are applied to the phantom with anomalies as well. The B_1^+ magnitude, F_x and EP reconstructions with cr-MREPT method for normal and modified drive, as well as the combined EP reconstructions are demonstrated in figure (5.8). As we scrutinize the B_1^+ magnitude of the modified drive in figure (5.8e), the existence of a high and low field region separation similar to the homogeneous phantom case becomes evident, though this separation is not as optimal as in the homogeneous case. On the other hand, figure (5.8b) and (5.8f) clearly demonstrate that also in the phantom with anomalies, the LCF regions are significantly shifted and do not overlap. In parallel with this observation, the LCF artifacts in the EP reconstructions are also shifted. When the combined reconstructions in figure (5.8i) and (5.8j) are examined, it is clear that both the LCF artifacts and global biases are significantly eliminated.

Although the RF amplitude and phase values in table (5.1), which are designed for the homogeneous phantom, are used for the phantom with anomalies, it became possible to sufficiently alleviate the LCF artifact and the global biases. Using the same modified input RF signals for different phantoms significantly facilitates the experimental process by getting rid of the need for another modification procedure for every object to be imaged inside the TEM array.

5.3.4 Head Model Results

The head model is simulated using the same RF magnitudes and phases as used in the previous phantom simulations. The B_1^+ magnitudes, F_x magnitudes and EP reconstructions the for normal and modified drive are demonstrated in figure (5.9).

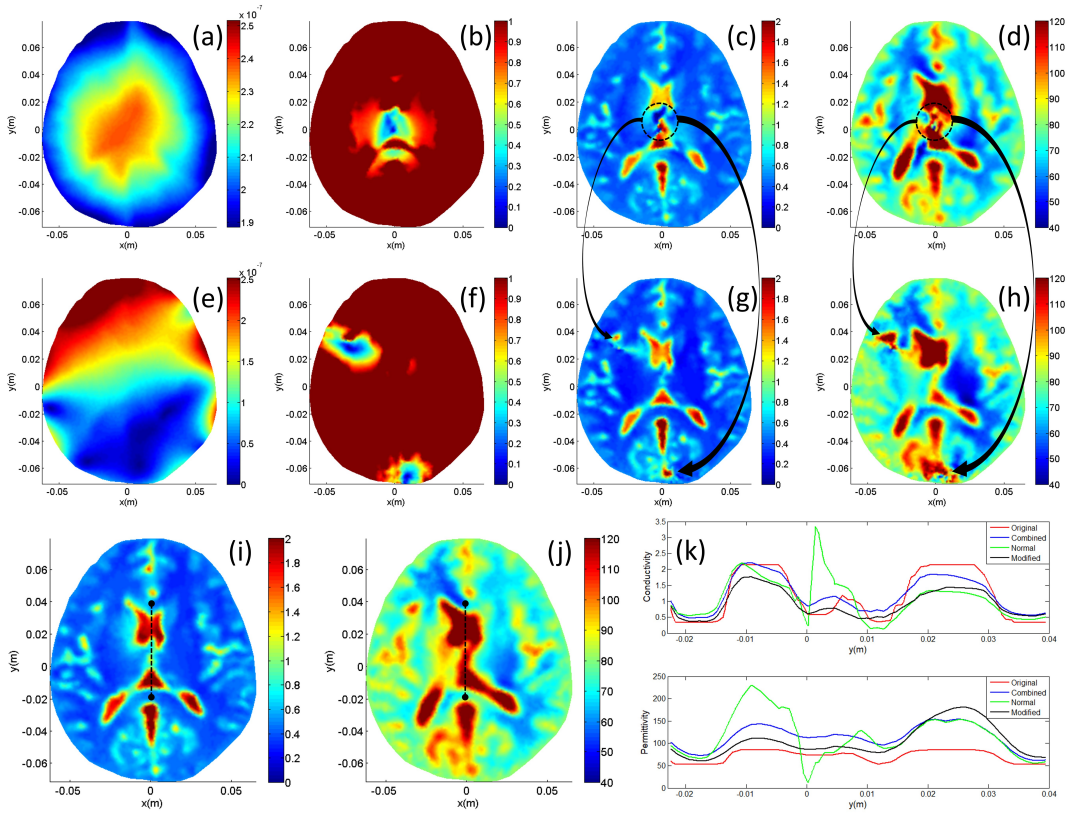

Figure 5.9: Head model results: (a,e): B_1^+ magnitude, (b,f): F_x magnitude, (c,g): conductivity reconstructions (S/m), (d,h): relative permittivity reconstructions for the normal and modified drive respectively, (i): combined conductivity reconstruction, (j): combined relative permittivity reconstruction and (k): Profile plots of original conductivity and relative permittivities (red) as well as profile plots of the reconstruction results for the normal drive (green), modified drive (black) and combined reconstruction (blue) cases. The profiles are taken along the dashed lines in (i) and (j).

Considering figure (5.9), it can be seen that the low convective fields occur at the center of the brain phantom for the normal drive case, being similar to the cylindrical phantoms. As figure (5.9e) is examined, it seems that the input RF sinusoids in table (5.1) provides the separation of high and low field regions even for the head model. Examining figure (5.9b) and figure (5.9f), the shift in LCF artifact when the modified drive is applied, can become clear. The combined solution shown in figure (5.9i) clearly demonstrates an improved conductivity reconstruction, being much more accurate than the solutions from individual

drives. Although the permittivity reconstructions of the normal drive have overestimated results at the CSF regions, just as reported in [20], the modified drive is able to shift the LCF artifact on the permittivity reconstructions as well, yielding artifact-free combined permittivity reconstructions. From the same figure, the profile plots along the dashed lines on (i) and (j) better show this situation.

The conductivity reconstructions of the head model actually finalizes the theory of the artifact elimination algorithm. A significant point of emphasis is that the same RF inputs can be used for different phantoms, and therefore, patient-specific B_1 shimming is not required. More detailed work such as boundary performance and noise analyses can be found in [37].

Chapter 6

Practical Implementation of the Method

The artifact elimination method in chapter (5) provides a novel solution to the LCF artifact of the cr-MREPT method in the framework of computer simulations. It serves as an enhancement procedure for the commonly known cr-MREPT method by using non-quadrature drive, which was referred to as the "modified drive" configuration. This chapter shows the effort and work to implement that method in the practical MRI environment. In this regard, there occurs an obstacle in the way of the practical implementation of the proposed method as it requires the retrieval of the transmit field (B_1^+) magnitude and phase distributions.

In this chapter, we propose a simpler method to determine the phase of the transmit field in an eight port microstrip transceiver TEM array for the case of non-quadrature excitation in $3T$. The proposed method requires a single additional quadrature driven MRI experiment. The developed ideas are tested in the framework of both simulations and MRI experiments with the use of four different non-quadrature drive configurations. It has been observed that the simulated and experimental - wise acquired transmit phase distributions tend to have a strong consensus which supports the validity of the proposed method.

Finally, the estimated transmit phase distribution for non-quadrature drive configuration is used in two different MR-EPT studies to get the conductivity reconstructions in order for the validation of its eligibility in MR-EPT studies.

6.1 Theory

In order for the retrieval of the transmit phase distribution, a deep understanding of the accumulated phase on a single channel of the transceiver array turns out to be an essential step. As mentioned, the proposed method uses a quadrature driven MRI sequence execution in addition to the non-quadrature drive, in order to extract the individual receive phase distributions of transceiver channels. These receive phases will be identical for both quadrature and non-quadrature excitation cases. Commencing with the theory of the accumulated phase on a single channel of the TEM array in a sequence execution, the step by step transmit phase retrieval procedure for quadrature and non-quadrature drive cases are given as in the following:

6.1.1 Accumulated Phase On a Single Channel of the TEM Array

The phase value at location $\boldsymbol{r}$ on the MRI image , being acquired by the i'th channel where $i \in \{1, 2, 3, ..., 8\}$ can be expressed as: [18, 35]

$$\Phi_i(\boldsymbol{r}) = \phi_{B_{1_i}^{-*}}(\boldsymbol{r}) + \phi_{B_1^+}(\boldsymbol{r}) + \phi_{(0,i)} + \phi_{\Delta B_0}(\boldsymbol{r}) + \phi_{res}(\boldsymbol{r}) \tag{6.1}$$

where, $\phi_{B_{1_i}^{-*}}(\boldsymbol{r})$ is the receive phase of the i'th channel, $\phi_{B_1^+}(\boldsymbol{r})$ is the phase of the transmit field when either all of the channels or only some channels are transmitting, and $\phi_{(0,i)}$ is the position independent zero-order phase contribution of the i'th channel being dependent on the connecting cable lengths, phase contribution of the receive amplifiers and the spatial position of the receiver

channel on the coil. The last two terms in equation (6.1), being $\phi_{\Delta B_0}(\boldsymbol{r})$ and $\phi_{res}(\boldsymbol{r})$ are the phase contribution due to B_0 and eddy currents respectively, whose effect will be neglected in our studies assuming that the the steady state free precession (SSFP) sequence is used [27].

6.1.2 Quadrature Drive B_1^+ Phase Retrieval

For the quadrature drive experiment, we propose the use of transceive phase approximation (TPA). However, the eight receive phases from eight channels need to be merged to converge on a single volume receive phase in order for the proper use of TPA.

The eight channel TEM array can also be used as a birdcage-like volume coil if during transmission, the channels are driven with 45 degrees of phase increments and during reception, the receive channel signals are combined with proper phase increments. These "proper" phase increments depend not only on the physical position of the receiving coil on the circular structure, but also on the receiver cable lengths, pre-amplifier phase responses and other additional phase increments from the RF front end components of the MRI system.

For quadrature excitation, the transceive phase of the volume coil configuration ($\phi_{B_1^{trc}}^{quad}(\boldsymbol{r})$) for an 8 channel TEM array can be calculated from the MRI images obtained from individual receive channels as in equation (6.2) when the residual phase terms and phase accumulation due to B_0 inhomogeneities are neglected:

$$\phi_{B_1^{trc}}^{quad}(\boldsymbol{r}) = arg\big(\sum_{k=1}^{8} \boldsymbol{p_k}(\boldsymbol{r}) e^{i(-\phi_{(0,k)})}\big) \tag{6.2}$$

where $\boldsymbol{p_k}(\boldsymbol{r})$ is the MRI image obtained via the k'th receive channel and $\phi_{(0,k)}$ is the zero order phase offset of the k'th channel, being mentioned in equation (6.1). Ideally, if the phase responses of the RF pre-amplifiers and receive cable lengths were precisely equivalent, this zero-order phase would only be dependent on the spatial position of the receiver element (receive channel) on the eight

channel TEM array. In that case, the phase differences between the adjacent channels would have been 45°. However, additional phase increments due to hand - made receive pre-amplifiers turn out to be significantly different, and therefore, estimating this additional phase offset for the individual channels is necessary. This estimation is accomplished by averaging the phase of a small region of interest (ROI) in the middle of the phantom with equation (6.3), as used in [35].

$$\phi_{(0,k)} \simeq arg\Big(\sum^{roi} \frac{\boldsymbol{p_k(r)}}{|\boldsymbol{p_k(r)}|}\Big) \tag{6.3}$$

Approximation of the zero-order phase terms in equation (6.3) originates from the notion that the transceive phases being acquired from each channel need to attain a common value in the middle of an electrical properties (EP) - wise symmetrical phantom during quadrature excitation [35]. Equation (6.2) makes the additional correction due to receive channel positions as well as due to the phase offsets of connection cables and receiver pre-amplifiers by arbitrarily setting the averaged phases from the center of the phantom to zero for all of the channels. Calculation of these zero - order phase terms for different channels needs to be done in the quadrature drive experiment and the same values should also be used in the non-quadrature drive experiments. After the volume transceive phase is calculated in equation (6.2), the volume transmit phase is approximated by the transceive phase approximation as in the following:

$$\phi^{quad}_{B_1^+}(\boldsymbol{r}) = \phi^{quad}_{B_1^{trc}}(\boldsymbol{r})/2 \tag{6.4}$$

This TPA approximated quadrature drive volume transmit phase will be used to calculate the receive phases of each individual channel as well as calculating the volume transmit phase of the non-quadrature drive.

6.1.3 Non-Quadrature Drive B_1^+ Phase Retrieval

After acquiring the TPA approximated transmit phase using the above procedure, as a by-product, the receive phase of the k'th channel can be calculated as:

$$\phi_{B_{1_k}^{-*}}(\boldsymbol{r}) = arg\left\{ \frac{exp\Big(i\phi_{B_{1_k}^{trc}}^{quad}(\boldsymbol{r})\Big)}{exp\Big(i\phi_{B_1^+}^{quad}(\boldsymbol{r})\Big)} \right\} \tag{6.5}$$

where $\phi_{B_{1_k}^{trc}}^{quad}(\boldsymbol{r})$ is the transceive phase, retrieved with k'th channel during the quadrature drive and $\phi_{B_1^+(\boldsymbol{r})}^{quad}$ is the quadrature drive volume transmit phase obtained by equation (6.4). These receive phases, being specific for each receive channel, will be identical for quadrature drive and non-quadrature drive experiments.

After the phase acquisition in the quadrature drive case, the volume transmit phase of the non-quadrature drive experiment ($\phi_{B_1^+}^{non-quad}(\boldsymbol{r})$) can be calculated using one of the receive channels with the following formula:

$$\phi_{B_{1_k}^+}^{non-quad}(\boldsymbol{r}) = arg\left\{ \frac{exp\Big(i\phi_{B_{1_k}^{trc}}^{non-quad}(\boldsymbol{r})\Big)}{exp\Big(i\phi_{B_{1_k}^{-*}}(\boldsymbol{r})\Big)} \right\} \tag{6.6}$$

where, $\phi_{B_{1_k}^{trc}}^{non-quad}(\boldsymbol{r})$ is the transceive phase acquired from the k'th channel during the non-quadrature drive experiment. It is expected that equation (6.6) would yield the same result, irrespective of the channel being used i.e. irrespective of the value of k, where $k \in \{1, 2, 3, ..8\}$. Therefore, the average of the transmit phases, found from eight channels can be used. This average is taken as in equation (6.7), realizing that fraction in equation (6.7) will have unit magnitude.

$$\phi_{B_1^+}^{non-quad}(\boldsymbol{r}) = arg\left\{ \sum_{k=1}^{8} \frac{exp\Big(i\phi_{B_{1_k}^{trc}}^{non-quad}(\boldsymbol{r})\Big)}{exp\Big(i\phi_{B_{1_k}^{-*}}(\boldsymbol{r})\Big)} \right\} \tag{6.7}$$

6.2 Methods

6.2.1 Simulations

Throughout the simulations, the developed eight-channel TEM array is used along with the phantom with anomalies. This time, the cylindrical anomalies have a conductivity of 1 S/m each and the background conductivity is set to 0.5 S/m.

Regarding the B_1 shimming operations, the phase-only optimization procedure, which was explained in the 5^{th} chapter was used, as having a magnitude and phase optimized RF input pattern turns out to be highly difficult in the practical MRI settings. In this procedure, the magnitudes of the RF inputs are forced to 1V and their phases are optimized.

The same optimization goal (with the high and low field regions) as in chapter (5) is used both in simulations and experiments. As the bottom part of the B_1^+ magnitude is the low field region, this is explicitly called as the "Bottom Shadowed" excitation configuration. The other non-quadrature drive configurations are the rotated versions of the bottom shadowed drive and called as the "Right", "Left", and "Top" shadowed excitation configurations whose RF input phases are demonstrated in table (6.1).

	ϕ_1	ϕ_2	ϕ_3	ϕ_4	ϕ_5	ϕ_6	ϕ_7	ϕ_8
Quad	0	45	90	135	180	225	270	315
Right Sh	46.22	133.19	-147.08	-54.38	26.39	19.33	19.41	-43.10
Top-Right Sh.	133.19	-147.08	-54.38	26.39	19.33	19.41	-43.10	46.22
Top Sh	-147.08	-54.38	26.39	19.33	19.41	-43.10	46.22	133.19
Left Sh	26.39	19.33	19.41	-43.10	46.23	133.19	-147.08	-54.38

Table 6.1: The RF input phases for the quadrature drive and the four non-quadrature drive configurations: Top Shadowed, Top-Right Shadowed, Left Shadowed and Right shadowed.

6.2.2 MRI Experiments

During the experiments, transmission and reception are accomplished with the aforementioned hand-made RF front end, which is driven with an eight channel transmitter array of Siemens Tim Trio 3 T MRI scanner. Peak RF amplitudes of every channel is set to 100 V and it is reduced by the scanner due to SAR requirements. The transmit phase offsets for quadrature and four non-quadrature drive cases are the same as the ones in simulations and they are shown in table (6.1). For all of the experiments including quadrature and non-quadrature excitation configurations, magnitude of the transmit field ($|B_1^+|$) was found by the double angle method [32]. SSFP sequence was used for the retrieval of the transmit phases with the proposed method. In fact, the MRI sequence parameters are the same as the ones used in the initial experiments of the TEM array, given in table (4.1).

The transmit phase ($\phi_{B_1^+}$) is used in two different MR-EPT techniques to reconstruct the conductivity within the phantom: First one is the Helmholtz's equation based standard (conventional) MR-EPT [17] and the second one is the cr-MREPT method [20]. Regarding the combined cr-MREPT reconstructions, which are found by the developed method in the 5^{th} chapter, the B_1^+ data of top shadowed and quadrature drive are used. On the other hand, the upper part of the B_1^+ data ($y > 0$) is not used as the "shadowed" part of the non-quadrature drive is highly corrupted by noise.

6.3 Results

6.3.1 Receive Phases and Non-Quadrature Transmit Phases

The receive phases of each individual channel, being independent of the driving configuration, are demonstrated in figure (6.1). These phases were found with

equation (6.5). Furthermore, the transmit phase distributions, being calculated from each channel with equation (6.6) are also demonstrated on the same figure. As it can be seen in figure (6.1), the receive phase distributions tend to have a rotational variation among adjacent channels. The acquired transmit phases with each individual channel are almost identical, as expected. Just as stated in the theory section, taking the average of the transmit phase distributions, being found for different channels will improve the SNR, which will improve the MR-EPT reconstructions in this paper.

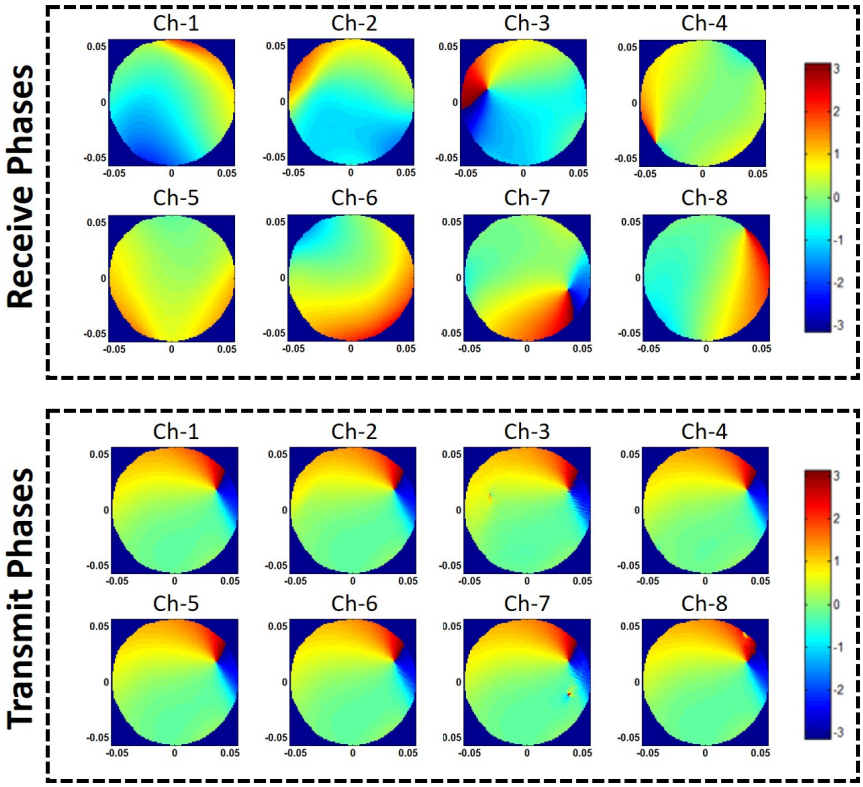

Figure 6.1: Receive phases of channels 1 to 8 are demonstrated in the first box. In the second box, the transmit phases, obtained from each channel is depicted. It should be noticed that the transmit phases are almost equivalent for each channel, as expected.

6.3.2 SSFP Magnitude, B_1^+ Magnitude and Transmit Phases

The channel-combined SSFP magnitude, B_1^+ magnitude and B_1^+ phase images for the quadrature and also the non-quadrature (i.e. Top, Right, Left, Top-Right shadowed) drives are demonstrated in figure (6.2).

Considering the quadrature drive, it can be observed that the B_1^+ magnitude image has a central brightening pattern, being slightly disturbed by the conductive anomalies of the phantom. The magnitude intensity of the SSFP image has increasing intensities at the top left and bottom right parts, due to different gains from hand-made receive pre-amplifiers. The experimental transmit phase image of the quadrature drive, found by equation (6.4) demonstrates a classical phase pattern, having a paraboloid shape. It is also observed that the simulated transmit phase has a very similar pattern.

For the non-quadrature drive cases, noise dominates in the regions where B_1^+ is low and SNR is not at acceptable levels. The experimental-wise found non-quadrature transmit phase estimations, depicted in figure (6.2) are very similar to the ones found in simulations. As it can be seen, there occurs point-wise phase excursions in the regions where B_1^+ magnitude significantly drops.

It needs to be recalled that the driving configurations of the non-quadrature drive cases are the rotated versions of each other. Therefore, the transmit phases of these excitation configurations need to be the rotated and phase-incremented version of each other [35]. It is important that this expectation is verified using experimental data.

In order to verify this phenomenon in MRI experiments, appropriate phases are added to the experimentally acquired transmit phases in left shadowed, top shadowed and top-right shadowed excitations. For instance, the drive pattern of left shadowed case is 180° rotated version of the right shadowed case. When we calculate the phase of $e^{j\phi_{leftsh}}e^{j\pi}$, we obtain the leftmost phase pattern in figure (6.2d). As expected, this phase pattern is 180° rotated version of right shadowed

transmit phase. When appropriate phases are added, this phenomenon is also observed in the Top Shadowed and Top-Right Shadowed configurations.

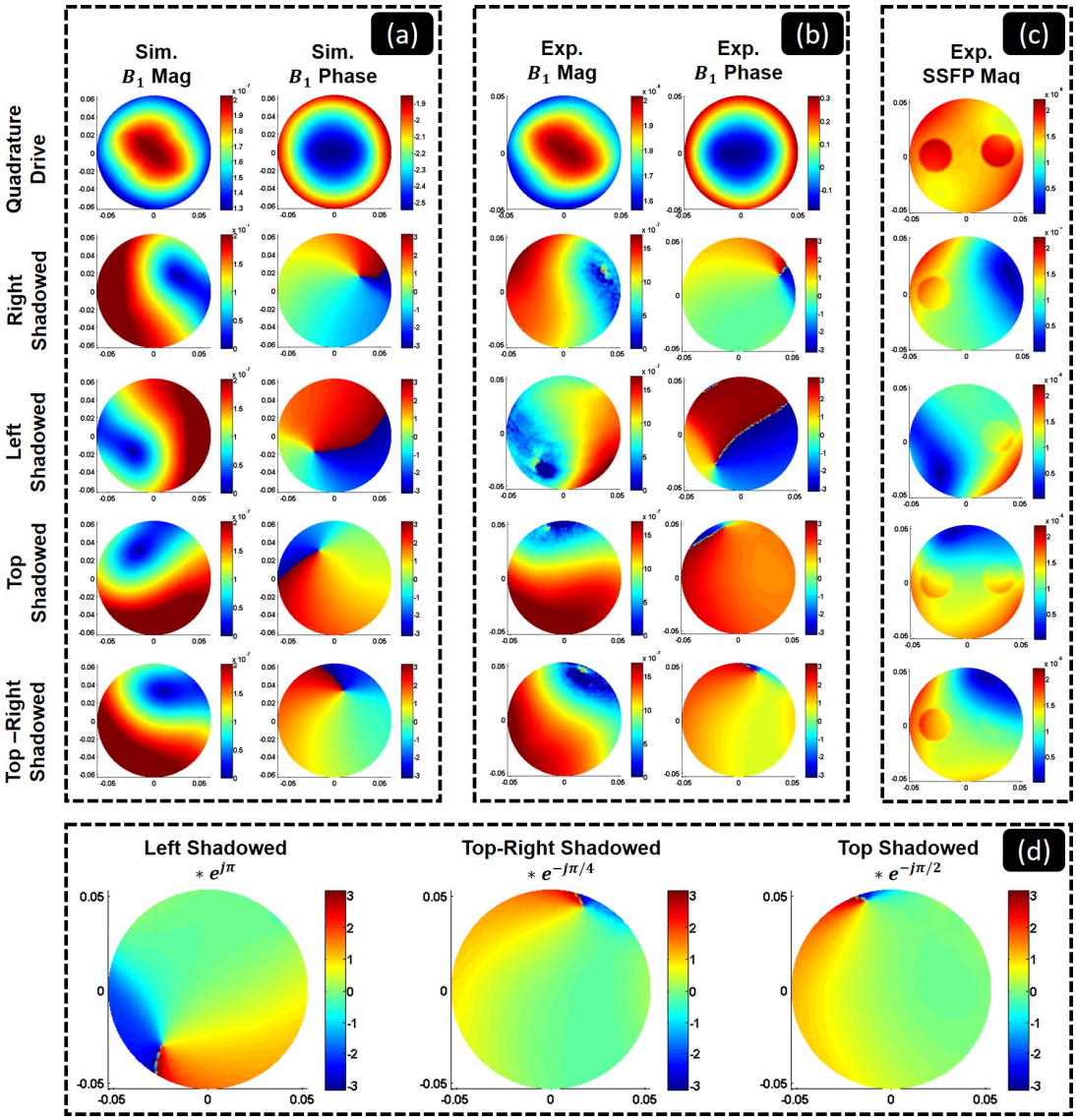

Figure 6.2: Simulated B_1^+ magnitude, simulated B_1^+ phase, experimental B_1^+ magnitude, experimental B_1^+ phase and SSFP magnitude images for all of the drive configurations. As it can be seen, the simulated B_1^+ phase distributions and experimental B_1^+ phase estimations are in a strong consensus.

6.3.3 Conductivity Reconstructions

The conductivity reconstructions with the standard (Helmholtz's equation based) MR-EPT and the cr-MREPT methods for the quadrature and non-quadrature drive configurations are shown in figure (6.3). To illustrate conductivity reconstructions of non-quadrature drive cases, the "top shadowed" and the "right shadowed" excitations are used. As expected, the locations in which the B_1^+ magnitude is low tend to be highly distorted.

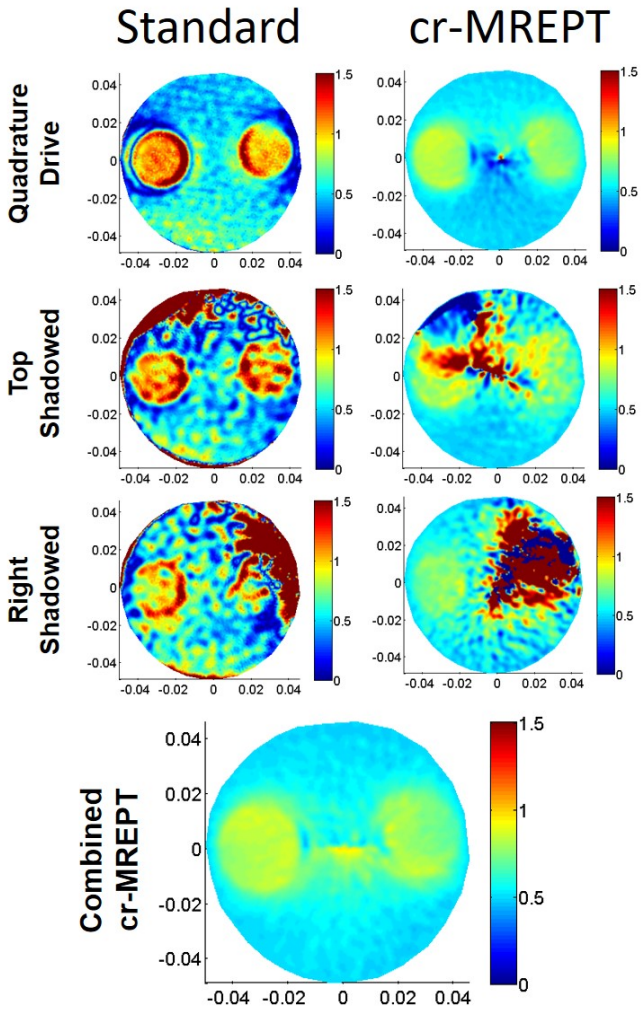

Figure 6.3: Experimental conductivity reconstructions: Helmholtz's equation based standard MR-EPT and cr-MREPT reconstructions of the quadrature drive, top shadowed and right shadowed excitation configurations.

Furthermore, the combined cr-MREPT results demonstrate that the LCF artifact is partially eliminated, being consistent with the simulations.

Considering the conductivity reconstructions, it should be stated that the reconstructions of the quadrature drive are highly accurate. On the other hand, the reconstructions made from non-quadrature drive tend to get highly corrupted at the low field regions because the B_1^+ magnitude at those regions are insufficient. This issue can be circumvented by increasing the B_1^+ magnitude throughout the entire slice. On the other hand, a professionally made RF front end and a stronger MRI transmitter array system is required for that. The imperfections of the currently used RF front end, unfortunately prevents us to use the magnitude and phase optimized RF input patterns and therefore, the LCF artifact cannot be completely eliminated.

Chapter 7

Final Remarks and Conclusions

Throughout this thesis, an improved cr-MREPT method has been proposed. In order to implement the proposed method, an eight channel decoupled TEM array has been designed and fabricated. Finally, the preliminary results of the proposed method have been given.

It should be thoroughly clarified that the designed and implemented eight channel TEM array constitutes the actual essence of this thesis. Not only it required us to learn a solid foundation of RF engineering techniques – including computational electromagnetic design tools, design of guiding structures, use of microwave test equipment– but it also served as a departure point for the development of the proposed artifact reduction algorithm.

Considering the performance of the head-sized array, it should be noticed that all of the ports are very aggressively and successfully matched to 50 Ω with L/C networks. Obviously, the performed impedance matching – including the use of very small and accurate capacitance values – is specific for this application as the matching bandwidth is very narrow. With the sufficient decoupling conditions, it became possible to acquire MRI images with very good SNR values and furthermore, the images were suitable for the use in MR-EPT applications.

The proposed algorithm for eliminating the LCF artifact is a solid step towards

the clinical feasibility of the cr-MREPT method. The simulation results show that it is a nice candidate for alleviating the global biases and LCF artifacts from the EP reconstructions. It has been shown that the same RF input pattern can be successful in homogeneous phantom, a phantom with anomalies, and a brain model. Therefore, the method can be applied in clinical studies without requiring an optimization process for every patient.

In order for implementing the proposed method, retrieval of the transmit B_1^+ magnitude and absolute transmit phase ($\phi(B_1^+)$) turns out to be essential. Although measuring the magnitude is possible, there is still no straightforward method to obtain the absolute phase of the transmit (B_1^+) field in a non-quadrature excitation. Although not published yet, another method to estimate the transmit phase of non-quadrature drive experiments has also been provided. The promising consensus between simulation and experimental results strongly supports the accuracy of the phase estimations.

Finally, the preliminary experimental results of the proposed algorithm has been given. On the other hand, the LCF artifact has not been fully recovered as the desired RF transmission could not be applied. However, when the physical limitations of the transmitter array system of the MRI Scanner and the use of an entirely hand-made RF front-end, including the TEM array is considered, the final conductivity results turn out to be highly promising.

In order for a fully artifact-free EP reconstruction, therefore, use of a professionally made RF front-end and a transmit array, which can provide higher RF input powers, can be suggested. Not only will it increase the overall SNR of the conductivity reconstructions, but also it will enable us to use the desired RF inputs in the non-quadrature excitation.

Appendix A

RF Front End Measurements

The RF front end system, including the transmit cables and RF Switch, designed by Taner Demir needs to be driven with the input phase offsets to get a phase of zero at the transmit output of the switch. These offsets are given in table (A.1).

	Ch1	**Ch2**	**Ch3**	**Ch4**	**Ch5**	**Ch6**	**Ch7**	**Ch8**
Zero	189	158	232	243	186	295	165	0
Cw-Pol	234	248	7	63	51	205	120	0
C-Cw-Pol	144	68	97	63	321	25	210	0

Table A.1: RF phase offsets to get the same RF phase at the coil-end output of the RF switch are demonstrated with the entry "Zero". Cw-Pol is input phase offsets to get a quadrature drive with an eight channel transmit coil. C-Cw-Pol is the input phase offsets to get a counter-clockwise circularly polarized B_1^+ field.

Gains ($|S_{21}|$) and phase responses $\phi(S_{21})$ of the RF pre-amplifiers are measured with an input power level of -20 dBm and are given in table (A.2):

	Ch1	**Ch2**	**Ch3**	**Ch4**	**Ch5**	**Ch6**	**Ch7**	**Ch8**
$\boldsymbol{\lvert S_{21}\rvert}$ **(dB)**	19.8	18.8	24	19	20	20	20	19.7
$\boldsymbol{\phi(S_{21})}$ **(degree)**	-15	-20	-27	-10	-31	-31	-28	-37

Table A.2: Forward gains ($|S_{21}|$) and phase responses $\phi(S_{21})$ of the RF pre-amplifiers.

Bibliography

[1] J. T. Vaughan, H. P. Hetherington, J. O. Otu, J. W. Pan, and G. M. Pohost, "High Frequency Volume Coils for Clinical NMR Imaging and Spectroscopy," *Magnetic Resonance in Medicine*, vol. 32, pp. 206–218, 1994.

[2] J. T. Vaughan and J. R. Griffiths, *RF Coils for MRI*. Wiley, 2012.

[3] A. S. Tarakameh, *Design of a Birdcage-Like Radio Frequency Transmit Array Coil for the Magnetic Resonance Imaging Using Equivalent Circuit Model*. PhD thesis, Bilkent University, 2016.

[4] J. Nistler, R. Kurth, R. Lazar, M. Vester, and W. Renz, " A Degenerate Bandpass Birdcage as Antenna for a 3T Wholebody Transmit Array ," in *Proceedings of the 14th Annual meeting of ISMRM*, (Seatle, WA, USA), 2006.

[5] P. Vernickel *et al.*, "Eight-Channel Transmit/Receive Body MRI Coil at 3T," *Magnetic Resonance in Medicine*, vol. 58, pp. 381–389, 2007.

[6] A. J. Surowiec, S. S. Stuchly, J. R. Barr, and A. Swarup, "Dielectric Properties of Breast Carcinoma and the Surrounding Tissues," *IEEE Transactions on Biomedical Engineering*, vol. 35, no. 4, pp. 257–263, 1988.

[7] W. T. Joines, Y. Zhang, L. Chenxing, and L. Jirtle, "The Measured Electrical Properties of Normal and Malignant Human Tissues from 50 to 900 MHz," *Med. Phys.*, vol. 21, no. 4, pp. 547–550, 1994.

[8] D. S. Holder, "Detection of Cerebral Ischaemia in the Anaesthetised Rat by Impedance Measurement with Scalp Electrodes: Implications for Non-Invasive Imaging of Stroke by Electrical Impedance Tomography,"

Clinical Physics and Physiological Measurement, vol. 13, no. 1, pp. 63–75, 1993.

[9] Z. Liu *et al.*, "Noninvasive Reconstruction of Three-dimensional Ventricular Activation Sequence from the Inverse Solution of Distributed Equivalent Current Density," *IEEE Transactions on Medical Imaging*, vol. 25, no. 10, pp. 1307–1318, 2006.

[10] B. He *et al.*, "Electrophysiological Imaging of Brain Activity and Connectivity-Challenges and Opportunities," *IEEE Transactions on Medical Imaging*, vol. 58, no. 7, p. 1918–1931, 2011.

[11] S. Gabriel *et al.*, "The Dielectric Properties of Biological Tissues: III. Parametric Models for the Dielectric Spectrum of Tissues," *Physics in Medicine and Biology*, vol. 41, no. 11, p. 2271–2293, 1996.

[12] A. Romsauerova, A. McEwan, L. Horesh, R. Yerworth, R. H. Bayford, and D. S. Holder, "Multi-Frequency Electrical Impedance Tomography (EIT) of the Adult Human Head: Initial Findings in Brain Tumours, Arteriovenous Malformations and Chronic Stroke, Development of an Analysis Method and Calibration," *Physiological Measurement*, vol. 27, pp. 147–161, 2006.

[13] O. Birgul and Y. Z. Ider, "Use of Magnetic Field Generated by the Internal Distribution of Injected Currents for Electrical Impedance Tomography," in *Proc. of IXth International Conference on Electrical Bio-Impedance in conjunction with European Concerted Action on Impedance Tomography*, (Heidelberg), pp. 418–419, 1995.

[14] Y. Z. Ider and O. Birgul, "Use of the Magnetic Field Generated by the Internal Distribution of Injected Currents for Electrical Impedance Tomography (MR-EIT)," *Turkish J. of Electrical Eng. And Computer Sciences*, vol. 6, no. 3, pp. 215–225, 1998.

[15] H. Griffiths, "Magnetic Induction Tomography," *Measurement Science and Technology*, vol. 12, p. 1126–1131, 2001.

[16] J. Liu, Y. Wang, U. Katscher, and B. He, "Electrical Properties Tomography Based on B_1 Maps in MRI: Principles, Applications and Challenges," *IEEE Transactions on Biomedical Engineering*, 2017. 10.1109/TBME.2017.2725140.

[17] T. Voigt, U. Katscher, and O. Doessel, "Quantitative Conductivity and Permittivity Imaging of the Human Brain Using Electric Properties Tomography," *Magnetic Resonance in Medicine*, p. 456–466, 2011.

[18] A. L. H. M. W. Van Lier *et al.*, "B_1^+ Phase Mapping at 7T and its Application for In Vivo Electrical Conductivity Mapping," *Magnetic Resonance in Medicine*, vol. 67, pp. 552–561, 2012.

[19] A. Nachman, D. Wang, W. Ma, and M. Joy, "A Local Formula for Inhomogeneous Complex Conductivity as a Function of the RF Magnetic Field," in *Proceedings of the 15th Annual meeting of ISMRM*, (Berlin, Germany), 2007.

[20] F. S. Hafalir, O. F. Oran, N. Gurler, and Y. Z. Ider, "Convection-Reaction Equation Based Magnetic Resonance Electrical Properties Tomography (cr-MREPT)," *IEEE Transactions on Medical Imaging*, vol. 33, no. 3, p. 456–466, 2014.

[21] N. Gurler and Y. Z. Ider, "Gradient- Based Electrical Conductivity Imaging Using MR Phase," *Magnetic Resonance in Medicine*, vol. 77, pp. 137–150, 2016.

[22] J. Liu *et al.*, "Gradient-Based Electrical Properties Tomography (gEPT): A Robust Method for Mapping Electrical Properties of Biological Tissues In Vivo Using Magnetic Resonance Imaging," *Magnetic Resonance in Medicine*, vol. 74, pp. 634–646, 2015.

[23] E. Balidemaj *et al.*, "CSI-EPT: A Contrast Source Inversion Approach for Improved MRI-Based Electric Properties Tomography," *Ieee Transactions on Medical Imaging*, vol. 44, no. 9, pp. 1788–1796, 2015.

[24] J. E. C. Serralles *et al.*, "Global Maxwell Tomography: A Novel Technique for Electrical Properties Mapping Without Symmetry Assumptions or Edge Artifacts," in *Proceedings of the 24th Annual meeting of ISMRM*, (Singapore), 2017.

[25] A. Borsic, I. Perreard, A. Mahara, and R. J. Halter, "An Inverse Problems Approach to MR-EPT Image Reconstruction," *IEEE Transactions on Medical Imaging*, vol. 35, pp. 244–256, 2016.

[26] K. M. Ropella and D. C. Noll, "A Regularized, Model-Based Approach to Phase-Based Conductivity Mapping Using MRI," *Magnetic Resonance in Medicine*, vol. 78, pp. 2011–2021, 2017.

[27] U. Katscher *et al.*, "Determination of Electric Conductivity and Local SAR Via B_1 Mapping," *IEEE Transactions on Medical Imaging*, vol. 28, no. 9, pp. 1365–1374, 2009.

[28] C. Li, W. Yu, and S. Y. Huang, "An MR-Based Viscosity-Type Regularization Method for Electrical Property Tomography," *Tomography*, vol. 25, no. 1, pp. 50–59, 2017.

[29] G. Yildiz, G. Ariturk, and Y. Z. Ider, "Use of Padding to Eliminate Low Convective Field Artifact in Conductivity Maps Obtained by cr-MREPT," in *Proceedings of the 25th Annual meeting of ISMRM*, (Honolulu, HI, USA), 2017.

[30] N. Gurler, O. F. Oran, and Y. Z. Ider, "Combination of Multichannel Receive Data For Local Cr-MREPT," in *Proceedings of the 23th Annual meeting of ISMRM*, (Toronto, Ontario, Canada), 2015.

[31] N. Gurler, *Multichannel and Phase Based Magnetic Resonance Electrical Properties Tomography*. PhD thesis, Bilkent University, 2016.

[32] C. H. Cunningham, J. M. Pauly, and K. S. Nayak, "Saturated Double-Angle Method for Rapid B1 Mapping," *Magnetic Resonance in Medicine*, vol. 55, pp. 1326–1333, 2006.

[33] J. Liu, X. Zhang, S. Schmitter, P.-F. Van de Moortele, and B. He, "Determining Electrical Properties Based on B1 Fields Measured in an MR Scanner Using a Multi-channel Transmit/Receive Coil: a General Approach," *Physics in Medicine and Biology*, vol. 58, no. 13, 2013.

[34] J. Liu, P.-F. V. de Moortele, X. Zhang, Y. Wang, and B. He, "Simultaneous Quantitative Imaging of Electrical Properties and Proton Density From B_1 Maps Using MRI," *IEEE Transactions on Medical Imaging*, vol. 35, pp. 2064–2073, 2016.

[35] P. F. Van de Moortele *et al.*, "B_1 Destructive Interferences and Spatial Phase Patterns at 7 T with a Head Transceiver Array Coil," *Magnetic Resonance in Medicine*, vol. 54, pp. 1503–1518, 2005.

[36] U. Katscher, C. Findeklee, and T. Voigt, "B_1-Based Specific Energy Absorption Rate Determination for Nonquadrature Radiofrequency Excitation," *Magnetic Resonance in Medicine*, vol. 68, pp. 1911–1918, 2012.

[37] G. Ariturk and Y. Z. Ider, "Optimal multichannel transmission for improved cr-MREPT," *Physics in Medicine and Biology*, vol. 63, no. 4, 2018.

[38] D. M. Pozar, *Microwave Engineering*. Wiley, 2012.

[39] B. A. Baertlein *et al.*, "Theoretical Model for an MRI Radio Frequency Resonator," *IEEE Transactions on Biomedical Engineering*, vol. 47, no. 4, pp. 535–547, 2000.

[40] G. Adriany *et al.*, "Transmit and Receive Transmission Line Arrays for 7 Tesla Parallel Imaging," *Magnetic Resonance in Medicine*, vol. 53, pp. 434–445, 2005.

[41] G. Shajan, J. Hoffmann, J. Budde, G. Adriany, K. Ugurbil, and R. Pohmann, "Design and Evaluation of an RF Front-End for 9.4 T Human MRI," *Magnetic Resonance in Medicine*, vol. 66, pp. 596–604, 2011.

[42] C. A. T. Van den Berg *et al.*, "Simultaneous B_1^+ Homogenization and $Specific$ Absorption Rate Hotspot Suppression Using a Magnetic Resonance

Phased Array Transmit Coil," *Magnetic Resonance in Medicine*, vol. 57, pp. 577–586, 2007.

[43] R. Abraham and T. S. Ibrahim, "Proposed Radiofrequency Phased-array Excitation Scheme for Homogenous and Localized 7-Tesla Whole-body Imaging Based on Full-Wave Numerical Simulations," *Magnetic Resonance in Medicine*, vol. 57, pp. 235–242, 2007.

[44] N. Gurler and Y. Z. Ider, "Numerical Methods and Software Tools for Simulation, Design, and Resonant Mode Analysis of Radio Frequency Birdcage Coils Used in MRI," *Concepts in Magnetic Resonance*, vol. 45, no. 1, pp. 13–32, 2015.

[45] E. Michel, D. Hernandez, and S. Y. Lee, "Electrical Conductivity and Permittivity Maps of Brain Tissues Derived from Water Content Based on T1-Weighted Acquisition," *Magnetic Resonance in Medicine*, vol. 77, pp. 1094–1103, 2016.